Review Paper

Control and understanding of metal contacts to β-Ga_2O_3 single crystals: a review

Hogyoung Kim[1]

Received: 13 October 2021 / Accepted: 22 November 2021

Abstract

Gallium oxide (Ga_2O_3) is a promising semiconductor for high power devices and solar blind ultraviolet photodetectors due to its large bandgap, a high breakdown field, and high thermal stability. Recently, a considerable achievement has been obtained for the growth of high-quality β-Ga_2O_3 and high performance β-Ga_2O_3 based devices. However, rapid advance in device performance can be limited by the critical issues of metal contacts to β-Ga_2O_3 such as barrier height, leakage current, ohmic contact, and surface, interfacial and deep states. This article aims to provide a review on the recent studies in the control and understanding of metal contacts to β-Ga_2O_3, particularly in terms of the barrier formation. This review suggests that understanding the current transport mechanisms of metal contacts to β-Ga_2O_3 more thoroughly is necessary to enhance the performance, stability and reliability of β-Ga_2O_3 based devices.

Keywords Gallium oxide · Metal contacts · Barrier formation · Current transport mechanisms

1 Introduction

As an emerging semiconductor, β-Ga_2O_3 has attracted significant interest as next-generation high-power devices due to its wide bandgap (~ 4.85 eV) and theoretical critical field strength of 8 MV/cm [1]. High-performance power devices have been demonstrated in the form of Schottky barrier diodes [2–4] and field effect transistors (FTEs) [5–7]. Enhancing the device performance further as theoretically predicted requires high-quality epitaxial layer with low compensating defects and low background doping. In addition, β-Ga_2O_3 has been applied to other devices such as solar blind ultraviolet photodetectors [8], electroluminescent devices [9], window materials for optoelectronic devices [10], transparent conductive oxides [11], and hydrogen gas sensors [12].

Because of the highly asymmetric monoclinic crystal structure, β-Ga_2O_3 has known to have anisotropic material properties. Guo et al. found that thermal conductivity along the [010] direction is approximately three times larger than along the [100] direction [13]. Anisotropic nonlinear optical properties in β-Ga_2O_3 have been reported [14, 15]. Liu et al. grew β-Ga_2O_3 epilayers on *r*- and *c*-plane sapphire substrates and showed that β-Ga_2O_3 epilayers on *r*-plane revealed higher UV responsivity and detectivity [16]. Wong et al. reported an electron mobility anisotropy in β-Ga_2O_3 FETs, associated with the anisotropic carrier scattering [17]. Zhang et al. investigated the anisotropic etching behavior of β-Ga_2O_3 and showed that the wet etching in hot phosphoric acid could effectively reduce the sidewall roughness caused by plasma dry etching [18]. Jang et al. found that $(\bar{2}01)$ Ga_2O_3 had higher etch rates and could form ohmic contacts more easily than (010) Ga_2O_3, which was correlated with the higher density of oxygen dangling bonds on the $(\bar{2}01)$ plane [19]. Sasaki et al. found that the epitaxial growth rate for (100) plane

---

✉ Hogyoung Kim, hogyoungkim@gmail.com | [1]Department of Visual Optics, Seoul National University of Science and Technology (Seoultech), Seoul 01811, Republic of Korea.

| https://doi.org/10.1007/s42452-021-04895-9

was lower than (010) plane because of the low adhesion energy on the terraces for (100) surface [20]. Fu et al. comparatively investigated Schottky contact to $(\bar{2}\,01)$ and (010) β-Ga_2O_3 interfaces and found higher barrier height, lower reverse leakage current, and larger breakdown voltage for (010) orientation [21]. Bhattacharyya et al. fabricated Schottky contacts to (010), $(\bar{2}\,01)$ and (100) β-Ga_2O_3 substrates and found that the barrier heights for (010) orientation are highest among three orientations [22]. These anisotropic material properties definitely give a significant impact on the β-Ga_2O_3 based device performance.

Metal–semiconductor (MS) Schottky contacts are utilized to investigate the nature of defects and their impact on the material quality and the electrical characteristics. MS contacts are classified into two categories, namely, Schottky and ohmic contacts. The barrier height in a metal contact to an n-type semiconductor is given by $\Phi_B = \Phi_M - \chi$, where Φ_M and χ are the metal work function and the electron affinity of the semiconductor (4.0 eV for β-Ga_2O_3 [1]), respectively [23]. The work functions for various metals are available in Ref. [24]. Electrical properties of metal/β-Ga_2O_3 contacts according to the β-Ga_2O_3 crystal orientation have been investigated. For example, Yao et al. investigated the Schottky metal dependent electrical properties of Schottky diodes on $(\bar{2}\,01)$ and (010) β-Ga_2O_3 [25]. Schottky barrier heights from current–voltage (*I*–*V*) and capacitance–voltage (*C*–*V*) methods of the five metals revealed little dependence on the metal work function. Lyle et al. fabricated Ti contacts on (010) and (001) β-Ga_2O_3 and observed higher barrier height for (010) plane [26]. Further research on MS contacts can enhance the performance of β-Ga_2O_3-based devices. In this paper, recent studies on the control and understanding of metal contacts to β-Ga_2O_3 single crystals has been reviewed.

2 Material properties of β-Ga_2O_3

Among different crystalline phases of Ga_2O_3, the monoclinic phase β-Ga_2O_3 has the best thermal stability, while other four phases (α-, γ-, δ-, and ε-Ga_2O_3) are metastable and can be transformed to β-Ga_2O_3 at high temperatures [1]. Hence, most studies are focused on β-Ga_2O_3. Figure 1a shows a schematic draw of the unit cell of β-Ga_2O_3 and Fig. 1b shows the (010) and $(\bar{2}\,01)$ planes which are most commonly used for device applications [19]. Table 1 summarizes the material characteristics of β-Ga_2O_3, GaN, 4H-SiC, diamond and Si. Except diamond, the bandgap and breakdown field of β-Ga_2O_3 are larger than other semiconductors. The Baliga's figure of merit (BFOM) for β-Ga_2O_3 is larger than GaN and 4H-SiC, highly beneficial to fabricate high-power electronic devices. However, relatively low thermal conductivity can cause self-heating effects. Excessive heat accumulation will degrade the performance and stability of the devices. Relatively low mobility also has a negative effect on the device characteristics.

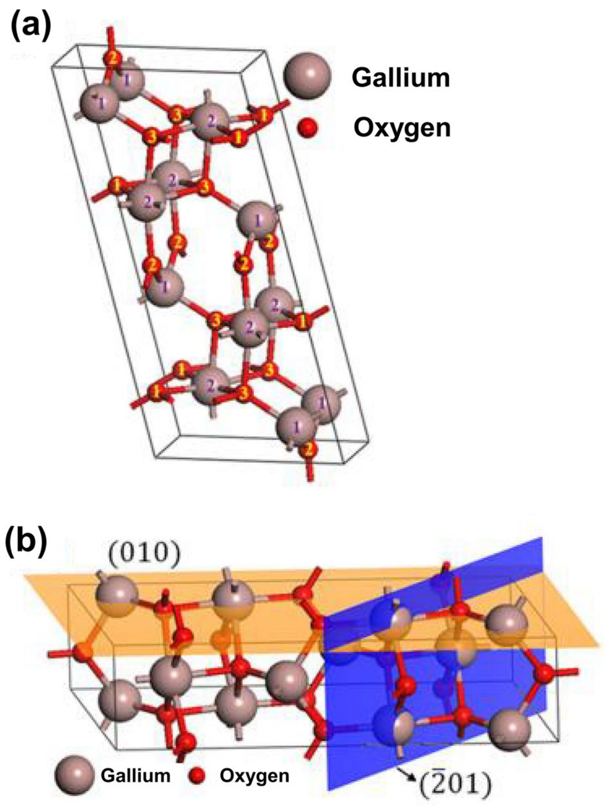

Fig. 1 **a** β-Ga_2O_3 crystal structure and **b** (010) and $(\bar{2}\,01)$ β-Ga_2O_3 surfaces [19]

Bulk Ga_2O_3 single crystals can be grown using the following methods: edge-defined film-fed growth (EFG) [27], Czochralski (CZ) [28, 29], Floating zone (FZ) [30] and vertical Bridgman (VB) [31]. Using the EFG method, Kuramata et al. [27] obtained a large and high-quality β-Ga_2O_3 single crystals up to 4 inches, with no twin boundaries and the dislocation density of ~ 10^3 cm^{-2}. Galazka et al. reported a two-inch-diameter cylindrical β-Ga_2O_3 single crystal grown by CZ method [29]. FZ method is utilized to grow β-Ga_2O_3 rod with a typical growth rate of 6 mm/h and a diameter of 10 mm [30]. VB method provides some advantage such that β-Ga_2O_3 single crystals are easily released after growth. Using VB method, Hoshigawa et al. obtained a 25-mm-diameter β-Ga_2O_3 single crystal [31]. Among these methods, the EFG method is considered to be the most promising technique to grow bulk β-Ga_2O_3, because of the capability of achieving large size and high quality bulk β-Ga_2O_3 for future high-volume production [32, 33]. Unintentionally doped (UID) n-type β-Ga_2O_3 single crystals are normally obtained due to the incorporation of Si and

Table 1 Material properties of β-Ga_2O_3 in comparison with those of GaN, 4H-SiC, Diamond and Si (Baliga's figure of merit: BFOM) [1]

Properties	GaN	4H-SiC	Diamond	β-Ga_2O_3	Si
Bandgap, E_g (eV)	3.4	3.25	5.5	4.85	1.1
E_c (MV/cm)	3.3	2.5	10	8	0.3
Dielectric constant, ε	9.0	9.7	5.5	10	11.8
Electron mobility, μ (cm^2/V·s)	1250	1000	2000	300	1480
BFOM ($\varepsilon\mu E_C^3$) relative to Si	846	317	24,660	3214	1
Saturation velocity (10^7 cm/s)	2.5	2	1	1.8 ~ 2	1
Thermal conductivity (W/cm·K)	2.3	3.8	20	0.1 ~ 0.3	1.5

Ir atoms from the β-Ga_2O_3 seed and crucible. Hence semi-insulating crystals are achieved by Mg or Fe doping acting as deep acceptors [32, 33].

Low-resistivity β-Ga_2O_3 substrates can be obtained by intentional doping, which are necessary to achieve better ohmic contacts and lower threshold voltages. For n-type dopants, Sn, Si, and Nb have been employed. Ohira et al. investigated the effect of the annealing process at 1100 °C on the material properties of Sn-doped β-Ga_2O_3 grown by the FZ method and found that their properties changed marginally [34]. Zhang et al. studied the effect of Sn doping in FZ-grown β-Ga_2O_3 crystals and reported an increase in the absorption coefficient with the Sn doping and a reduction in the absorption coefficient after annealing, associated with the decrease of free carriers [30]. Víllora et al. obtained Si-doped β-Ga_2O_3 grown by the FZ method with the Si concentrations of $10^{16} \sim 10^{18}$ cm^{-3} and showed that the conductivity can be intentionally controlled over three orders of magnitude by Si doping [35]. Based on the result, they suggested that electrical conductance of β-Ga_2O_3 is mainly governed by Si impurities and the contribution of oxygen vacancies, if any, is not significant. Zhou et al. grew Nb-doped β-Ga_2O_3 by the FZ method and could achieve the carrier concentration from 9.55×10^{16} to 1.8×10^{19} cm^{-3} [36]. In the case of p-type doping, Mg has been used as a dopant. Onuma et al. grew Mg-doped β-Ga_2O_3 crystals by the FZ method and observed the semi-insulating behavior for Mg concentration of 4×10^{18} -2×10^{19} cm^{-3} [37]. Based on the first-principles calculations, Dong et al. showed that N serves as a deep acceptor with an energy level of 1.33 eV above the valence band maximum, which is not effective as a p-type dopant [38]. Hence the achievement of p-type doped β-Ga_2O_3 remains a big challenge.

3 Schottky barrier diodes

Schottky barrier diodes can be electrically characterized using *I–V* and *C–V* methods to obtain Schottky barrier heights (SBHs). Assuming the thermionic emission (TE) model, the forward bias *I–V* characteristics of a Schottky diode are analyzed using the following equation [23]

$$J = A^{**}T^2 \exp(-q\phi_B/kT)[\exp\{q(V - IR_S)/nkT\} - 1] \quad (1)$$

where A^{**} is the effective Richardson constant (41.1 cm^{-2} K^{-2} for n-Ga_2O_3), $q\phi_B$ is the effective SBH, R_S is the series resistance, and n is the ideality factor. Both the barrier height and ideality factor are calculated from the linear part in ln(*I*)–*V* curves. The flat-band barrier height is obtained from the *C–V* characteristics under reverse bias condition. The capacitance in the Schottky diodes satisfies the following equation [23]

$$\frac{A^2}{C^2} = 2\left(\frac{V_b - V - kT/q}{qN_D\varepsilon_S\varepsilon_0}\right) \quad (2)$$

where V_b is the built-in potential, N_D is the carrier concentration, and ε_S the dielectric constant of semiconductor, and ε_0 is the vacuum permittivity. The carrier concentration is calculated from the slope of A^2/C^2 versus V plot. The barrier height is obtained from $q\phi_B^{(C-V)} = qV_0 + qV_n + kT$, where V_0 is the intercept of A^2/C^2 with the voltage axis, and $qV_n = E_C - E_F$. The SBH from *C–V* method is generally higher than that from *I–V* method. This is due to the nonuniform interfacial layer and the distribution of interfacial defects at the MS interface [39]. The obtained capacitance during the *C–V* measurement at high frequency is not sensitive to potential fluctuations for length scales smaller than the depletion width. In this case, the capacitance is the average value over the SBH values. In addition, the effect of image force lowering and tunneling on the current conduction is negligible under the flat-band condition because electric field in the semiconductor is zero. Thus, the SBHs determined from the *C–V* method are observed to be higher than those determined from the *I–V* method. The flat-band barrier heights can also be obtained using the ideality factor and the effective SBH obtained from the TE model [40]

$$\phi_{FB} = n\phi_{TE} - (n-1)\frac{kT}{q}\ln\left(\frac{N_C}{N_D}\right) \quad (3)$$

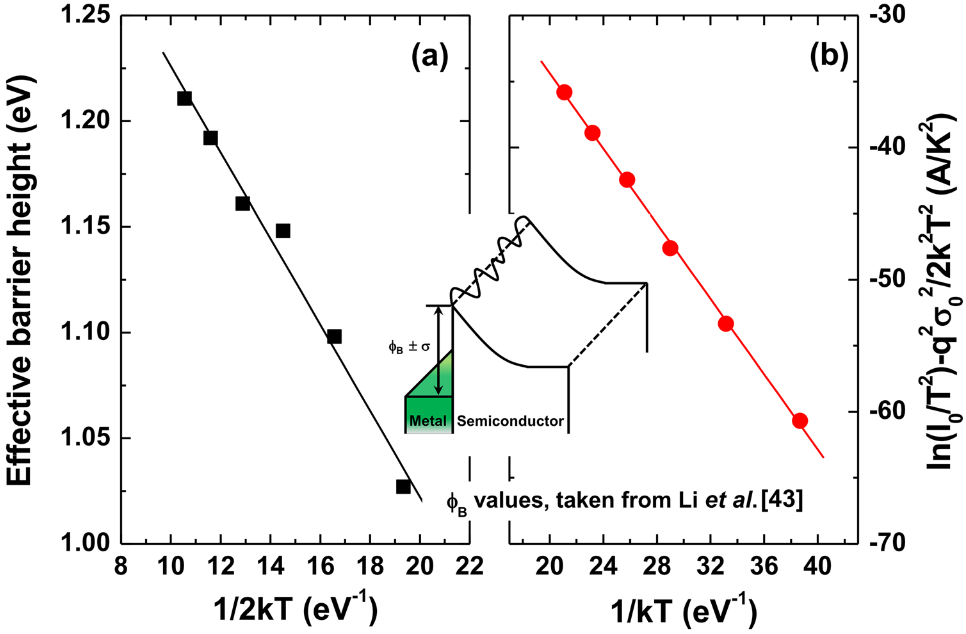

Fig. 2 **a** Plot of barrier height versus 1/2*kT* and **b** modified Richardson plot. The barrier heights at different temperatures were taken from Li et al. [43]. The inset in **a** shows a schematic band diagram of inhomogeneous Schottky barrier

where N_C is the density of states at conduction band. In identically prepared diodes on the same semiconductor, there exists normally a linear relationship between the effective SBH and the ideality factor. After obtaining the straight lines by fitting to the effective SBH versus ideality factor plots, laterally homogeneous Schottky barrier height ($q\phi_B^{\text{hom}}$) can be obtained from an extrapolation of these straight lines to the image-force controlled ideality factor n_{if} [41].

Analyses on the temperature dependent *I*–*V* characteristics can also be carried out, which are required for clarifying the origin of non-idealities in the Schottky barrier and attaining the detailed knowledge on the current transport mechanism and the properties of defects and the mechanism of barrier formation. One of the non-idealities is the temperature dependence of electrical parameters. For example, an increase in barrier height and a decrease in ideality factor are observed from the temperature dependent *I*–*V* characteristics, which are associated with the laterally inhomogeneous Schottky barrier [42]. A Gaussian distribution of barrier heights over the Schottky contact area is assumed in this model, where the effective SBH ($q\phi_B$) related with a zero-bias mean SBH ($q\overline{\phi}_B$) and a standard deviation (σ_0) is given by [42]

$$q\phi_B = q\bar{\phi}_B - q^2\sigma_0^2/2kT \tag{4}$$

Then, the modified Richardson plot can be obtained as follows

$$\ln\left(\frac{I_0}{T^2}\right) - \frac{q^2\sigma_0^2}{2k^2T^2} = \ln(AA^{**}) - \frac{q\phi_B}{kT} \tag{5}$$

Using Eq. (5), the modified Richardson constant (A^{**}) is calculated.

Li et al. reported an increase in barrier height with the temperature in Ni Schottky contacts to β-Ga$_2$O$_3$ [43]. Although they provided the SBH values at different temperatures, the Schottky barrier inhomogeneity was not examined using the modified Richardson plots. By taking the SBHs at different temperatures from their work [43], the characteristics of Schottky barrier in β-Ga$_2$O$_3$ were analyzed in this article. Based on the linear fit to the plot of $q\phi_B$ versus1/2*kT* shown in Fig. 2a, the value of $q\overline{\phi}_B = 1.42$ eV and $\sigma_0 = 0.143$ V were obtained. From the linear fitting to the modified Richardson plot of $\ln(I_0/T^2) - q^2\sigma_0^2/2k^2T^2$ versus 1/*kT* shown in Fig. 2b, the Richardson constant was calculated to be 35.7 Acm^{-2} K^{-2}. This is similar to the theoretical value of 41.1 Acm^{-2} K^{-2} for n-Ga$_2$O$_3$, indicating that the temperature dependence of barrier heights can be explained by the inhomogeneous Schottky barrier with a Gaussian distribution of barrier heights. Li et al. also showed that the forward *I*–*V* characteristics follow the thermionic field emission (TFE) model rather than TE [43]. The obtained barrier heights from TFE model were about 1.32 ~ 1.40 eV, which are similar to the $q\overline{\phi}_B$ value of 1.42 eV, assuring again the inhomogeneous Schottky barrier for the forward current characteristics. The inset in Fig. 2(a) shows a schematic diagram of inhomogeneous Schottky barrier.

4 Metal contacts to *β*-Ga_2O_3

4.1 Schottky contacts to *β*-Ga_2O_3

Normally Schottky contacts to *β*-Ga_2O_3 single crystals have been fabricated in vertical structure, in which Schottky and ohmic contacts are formed on the front and back surfaces of the samples, respectively. A *β*-Ga_2O_3 epitaxial layer was used in some studies (denoted as n-epi/n-bulk), while other studies used bulk *β*-Ga_2O_3 (denoted as n-bulk). Note that most of the research results were obtained by analyzing only one or two contact metals and a comprehensive investigation using various metal contacts to the same *β*-Ga_2O_3 layer is still lacking. Owing to the different material quality of *β*-Ga_2O_3 layer, carrier concentration, surface/interface states, and surface treatment, direct comparison between each work can result in incorrect conclusions. Hence, research results including multiple metals within the same study were discussed mainly in this article.

Table 2 shows the research results in the literature obtained from Schottky contacts to ($\bar{2}$ 01) *β*-Ga_2O_3. The reported barrier heights for Ni and Pt contacts are in the range of 0.9 ~ 1.6 eV. Investigation of Schottky diodes using multiple metal contacts were performed by Yao et al. [25] and Hou et al. [56]. The Schottky metal contacts for these two works were formed on EFG-grown Sn-doped ($\bar{2}$ 01) *β*-Ga_2O_3 single crystals. Based on the reported SBHs, the relationships between barrier height and metal work function in Schottky contacts to ($\bar{2}$ 01) *β*-Ga_2O_3 were obtained, which are shown in Fig. 3a. The barrier heights show little dependence on metal work function, indicating significant Fermi-level (FL) pinning. Such FL pinning was associated with native defects or interface states located at ~ 1.3 eV below the conduction band (E_C) [56]. Higher density of oxygen dangling bonds on the ($\bar{2}$ 01) plane was suggested as an origin of strong FL pinning. Hou et al. also reported that barriers heights of oxidized Schottky contacts were to be higher than their unoxidized metal counterparts [56]. However, the oxidized contacts also showed little correlation between barrier height and metal work function. The barrier heights of the oxidized Schottky contacts were pinned by another deep-level defect close to E_C–2.0 eV.

Table 3 shows the research results in the literature obtained from Schottky contacts to (001) *β*-Ga_2O_3. Si-doped epitaxial layers grown on Sn-doped *β*-Ga_2O_3 substrates were mainly examined in this orientation. Lingaparthi et al. explored the surface states on halide vapor phase epitaxy (HVPE) grown (001) *β*-Ga_2O_3 epilayers by determining the SBHs for different metal contacts using Cr, Cu, Ni, and Au [76]. Figure 3b shows the plots of barrier height versus metal work function using the data taken from Lingaparthi et al. [76]. For epi-1 sample (HVPE-grown Si-doped epitaxial layer with the carrier concentration of 2.5–3.2 × 10^{16} cm^{-3}), the barrier height was found to be nearly pinned at 1.2 ~ 1.35 eV, closely matched with the energy level of the oxygen vacancy [V_O(III)] state (E_V + 3.57 eV) in *β*-Ga_2O_3. Based on this result, they suggested that FL pinning is due to V_O-related surface states on (001) oriented *β*-Ga_2O_3 epitaxial layers. In contrast, the FL was observed to be weakly pinned on the bulk and epi-2 (improved Si-doped epitaxial layer with the concentration of 5.3–7.2 × 10^{16} cm^{-3}) (001) *β*-Ga_2O_3. The density of surface states for epi-1 sample was found to be higher than those for bulk and epi-2 samples, indicating the presence of higher density of V_O-related states on the *β*-Ga_2O_3 surface for epi-1 sample. In another work [77], they showed by simulation that deep donor type surface states (probably V_O) are responsible for lowering the barrier height and increasing the reverse leakage current. Based on the results they suggested that the oxygen vacancy generated in (001) *β*-Ga_2O_3 epitaxial layer during the HVPE growth process affected on the SBH and the electrical properties of (001) *β*-Ga_2O_3 based devices.

Tables 4 and 5 show the research results in the literature obtained from Schottky contacts to (100) and (010) *β*-Ga_2O_3, respectively. Studies on these orientations are rather sparse. Lyle et al. investigated six different Schottky metals to (100) *β*-Ga_2O_3 substrates [78]. Near-ideal average ideality factors (1.05–1.15) were found for Ti, Mo, Co, and Ni contacts, whereas higher ideality factors (~1.3) were observed for Pd and Au contacts. The electrical behavior of the Pd and and Au contacts were associated with the presence of spatially inhomogeneous Schottky barriers. Figure 4a shows the plots of barrier height versus metal work function using the data taken from Lyle et al. [78], revealing a strong correlation between the calculated barrier heights and the metal work functions. Similarly, Fig. 4b shows the plots of barrier height versus metal work function for (010) *β*-Ga_2O_3 Schottky contacts, where the data were taken from Yao et al. [25] and Farzana et al. [88]. The barrier height is observed to be dependent on the metal work function, suggesting that metal contacts to (010) *β*-Ga_2O_3 are not fully pinned. According to the comparative studies on the Schottky contact to ($\bar{2}$ 01) and (010) *β*-Ga_2O_3 interfaces by Fu et al. [21] and Bhattacharyya et al. [22], barrier heights were found to be higher for (010) orientation compared to ($\bar{2}$ 01) orientation. Figures 5a and b show the temperature-dependent *I*–*V* characteristics for ($\bar{2}$ 01) and (010) *β*-Ga_2O_3 Schottky diodes, respectively, reported by Fu et al. [21]. The obtained barrier heights in Figs. 5c and d show the higher values for (010) orientation. These works indicate that the crystalline anisotropy

Table 2 Summary of Schottky contacts to $(\bar{2}01)$ β-Ga_2O_3 reported in the literature

Schottky contact (thickness: nm)	Ohmic contact (thickness: nm)	Schottky contact deposition	Device structure (Growth method)	$q\phi_B$ (eV)	Ideality factor	Cleaning method	Carrier concentration (cm^{-3})	Refs
Ni/Au (20/80)	Ti/Au (20/80)	E-beam evaporation	n-epi/n$^+$-bulk (MOCVD/EFG)	1.22 (*I–V*)	1.07	Patterned by lift-off	4.02×10^{15}	[44]
Ni/Pt (50/30)	Ti/Au (75/150)	E-beam evaporation	n$^+$-bulk	~ 1.2 (*I–V*)	1.14	Ozone, BOE (30:1), diluted HCl (1:1)	1.45×10^{18}	[45]
Ni	Ti (100)	Sputtering	n-bulk (EFG)	1.04 (*I–V*) 1.12 (*C–V*)	1.19	Solvent, Piranha	2.8×10^{17}	[46]
Pt/Au	Ti/Al/Ti/Au	E-beam evaporation	n$^+$-bulk (EFG)	0.94	1.39	Solvent	$\sim3\times10^{18}$	[47]
Ni/Au (20/80)	Ti/Au (20/80)	E-beam evaporation	n-bulk (EFG)	1.20 (*I–V*)	1.00	Plasma etching	$\sim3\times10^{17}$	[48]
Pt/Ti/Au (50/10/100)	Ti/Au (20/100)	E-beam evaporation	n-bulk (EFG)	1.20 (*I–V*)	1.02	Solvent, $HCl:H_2O$ for ohmic contact	-	[49]
Ni/Au (20/80)	Ti/Au (20/80)	E-beam evaporation	n-epi/n$^+$-bulk (MOCVD/EFG)	1.07 (*I–V*)	1.30	Patterned by lift-off	$\sim9\times10^{16}$	[50]
Pt/Au (20/80)	Ti/Au (20/80)	E-beam evaporation	n-bulk (EFG)	1.04 (*I–V*)	1.28	Patterned by lift-off	$\sim3\times10^{17}$	[50]
Pt/Au (20/200)	Ti/Au (10/100)	E-beam evaporation	n-bulk (EFG)	1.01 (*I–V*)	1.07	UV/ozone	$\sim3\times10^{17}$	[51]
TiN (65)	Ti/Au (10/100)	Atomic layer deposition	n-bulk (EFG)	0.98 (*I–V*)	1.09	UV/ozone	$\sim3\times10^{17}$	[51]
Graphite carbon/Pt (40/20)	Ti/Au (20.30)	Ion-beam sputtering	n-bulk (EFG)	0.8 ~ 1.2 (*I–V*) 1.6 (*C–V*)	1.08	Patterned by lift-off	2×10^{17}	[52]
Oxidized Pd (110)	Ti/Au (50/50)	Magnetron sputtering	n-bulk (EFG)	1.45 (*I–V*)	~ 1.1	Solvent	1.3×10^{17}	[53]
Ni/Au (150/200)	Ti/Al/Ti/Au (20/130/20/50)	E-beam evaporation	n$^+$-bulk (EFG)	~ 0.9 (*I–V*)	~ 1.5	Patterned by lift-off	5.5×10^{18}	[54]
W/Au (100/50)	Ti/Au (20/80)	DC sputtering/ E-beam evaporation	n-bulk (EFG)	0.97 (*I–V*) 0.92 (*I–V–T*)	1.04	HCl/ozone	2×10^{17}	[55]
Ru (~ 40)	Ti/Au (50/50)	RF sputtering	n-bulk (EFG)	1.05 ~ 1.2 (*I–V*), 1.26 (*C–V*)	1.05 ~ 1.15	-	1.3×10^{17}	[56]
Ni/Au	-	evaporation	n-bulk (EFG)	1.25 (*I–V*)	1.01	-	$\sim1.2\times10^{17}$	[57]
Ni/Au (20/80)	Ti/Au (20/80)	E-beam evaporation	n-bulk (EFG)	1.20 (*I–V*)	1.00	ICP etching	$\sim3\times10^{17}$	[58]

^{a}Carrier concentration for the layer on which the Schottky contacts are formed, ^{b}Growth method: Metal organic chemical vapor deposition (MOCVD), Edge-defined film-fed growth (EFG), MOCVD/EFG: MOCVD-grown epilayer on EFG-grown substrate

of β-Ga_2O_3 can affect the electrical properties of Schottky contacts and needs to be taken into account for device design.

Surface treatment prior to metallization is an important factor in determining the SBH and the device stability. Yao et al. investigated the effect of five different wet chemical treatments on the electrical properties of Ni/$(\bar{2}01)$ β-Ga_2O_3 Schottky diodes and found that rinsing in an organic solvent, cleaning with HCl and H_2O_2, and rinsing with deionized water showed the best results [25]. Based on the results they concluded that unpassivated surface states and/or bulk/near-surface defects are more dominant in determining the electrical behavior of these diodes compared to the choice of different Schottky metals. Yang et al. characterized the effect of various surface treatments such as gaseous (ultraviolet/O_3), liquid (HCl, buffered oxide

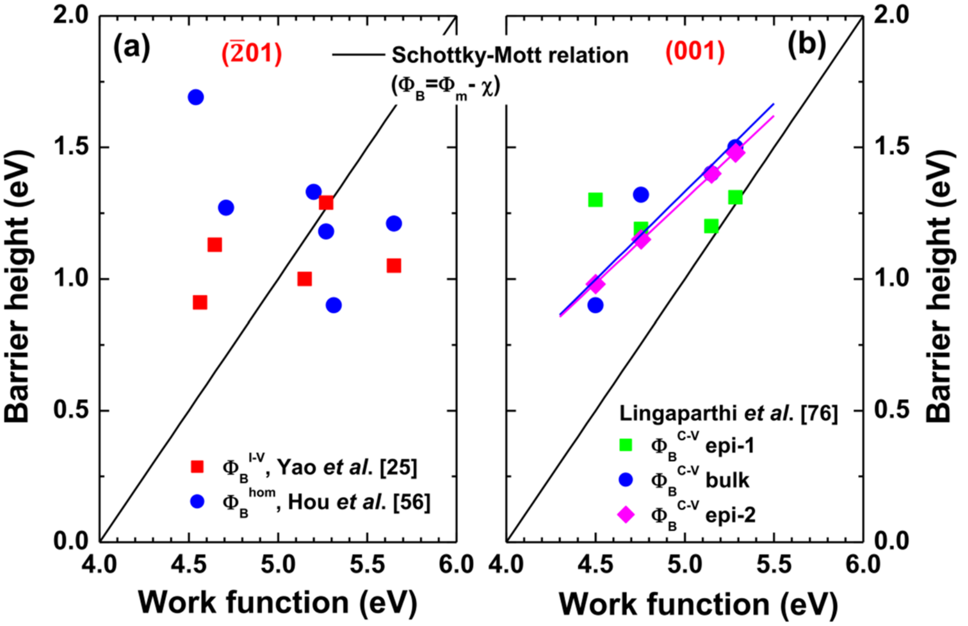

Fig. 3 Plots of barrier height versus metal work function for **a** $(\bar{2}01)$ β-Ga_2O_3 Schottky contacts using the barrier heights taken from Yao et al. [25] and Hou et al. [56] and **b** (001) β-Ga_2O_3 Schottky contacts using the barrier heights taken from Lingaparthi et al. [76]. The metal work functions were taken from ref. [24]

etch), or plasma (CF_4 and O_2) on the properties of Ni/(001) β-Ga_2O_3 Schottky diodes [94]. Standard chemical cleaning involving UV/O_3 or acid was found not to degrade the near-surface electrical properties whereas plasma treatment induced surface damage acting as generation-recombination centers. To date, however there is limited work on such systematic investigation using various surface treatments for the same β-Ga_2O_3 surface.

According to the review on Schottky contacts to β-Ga_2O_3, we can summarize the following points. (1) Significant FL pinning is observed for the Schottky contacts to $(\bar{2}01)$ β-Ga_2O_3 due to presence of surface and/or near surface defects. The possible origin of such defects is suggested to be oxygen vacancy-related defects. (2) Correlations between the barrier height and metal work function are observed for (001), (100) and (010) β-Ga_2O_3, suggesting that metal work function affects the barrier height on these orientations. (3) Compared to $(\bar{2}01)$ β-Ga_2O_3, (010) β-Ga_2O_3 revealed higher barrier height, associated with the larger surface band bending [21]. (4) When the surface defects are generated during the epitaxial growth, the FL pinning can occur [76]. Therefore, optimizing growth conditions for β-Ga_2O_3 epitaxial layer is pivotal to improve the device performance. (5) Mostly Schottky metals were deposited by using e-beam evaporation. For other semiconductors (e.g., GaN [95]), different barrier heights were obtained according to the deposition methods. This point needs to be explored for β-Ga_2O_3 Schottky diodes more thoroughly.

As a modulating method for diode characteristics, an interfacial layer (IL) between metal and β-Ga_2O_3 was proved to yield useful results. He et al. formed about 4 nm thick Al_2O_3 IL between Ni/Au and $(\bar{2}01)$ β-Ga_2O_3 substrate by annealing the sputtered Al layer at 300 °C in O_2 atmosphere [96] and observed the improved diode characteristics, with respective to the sample without IL. Further, they showed that this Al-reacted IL exhibited better performance than the sample with the Al_2O_3 IL prepared by atomic layer deposition (ALD). Harada and Tsukazaki deposited $PdCoO_2$ layer on $(\bar{2}01)$ β-Ga_2O_3 substrate by pulsed laser deposition (PLD) and fabricated the stacked Schottky contacts composed of various metals (Pt, Ni, Cr, and Ti) [97]. As shown in Fig. 6, they found that the barrier height systematically increased from 0.7 to 1.9 eV with the increase in the thickness of $PdCoO_2$ from 0 to 20 nm by selecting suitable combination of top metal and thickness of $PdCoO_2$. The $PdCoO_2$ layer consisted of alternatingly stacked ionic Pd^+ and $[CoCo_2]^-$ sublattices, which spontaneously induced interface dipoles that increased the SBH in β-Ga_2O_3 Schottky diodes. Bhattacharyya et al. deposited about 3 nm thick SiO_2 IL by ALD on (010), $(\bar{2}01)$ and (100) β-Ga_2O_3 substrates and observed the increase in barrier height for all orientations [22]. Especially, the Schottky contacts to (100)-oriented substrates exhibited a dramatic increment in barrier height and a reduction in reverse leakage current. These works suggest a strong potential of IL as a method to modulate the diode characteristics, however, these kinds of works are hardly observed.

The strong light absorption of metal contacts can limit the development of β-Ga_2O_3 Schottky-junction-based photonic devices. Due to the excellent properties such as high optical transmittance, large electrical conductivity, and a tunable work function, graphene is a good

Table 3 Summary of Schottky contacts to (001) β-Ga_2O_3 reported in the literature

Schottky contact (thickness: nm)	Ohmic contact (thickness: nm)	Schottky contact deposition	Device structure (Growth method)	$q\phi_B$ (eV)	Ideality factor	Cleaning method	Carrier concentration (cm^{-3})	Refs
Ni/Au (40/160)	Ti/Au (20/80)	E-beam evaporation	n-epi/n^+-bulk (HVPE/EFG)	1.03 (*I–V*)	1.1	Ozone, BOE	2.1×10^{15}	[59]
Ni/Au (40/160)	Ti/Au (20/80)	E-beam evaporation	n-epi/n^+-bulk (HVPE/EFG)	1.04 (*I–V*)	1.02	Ozone, BOE	1.33×10^{16}	[60]
Pt/Ti/Au (20/100/100)	Ti/Al/Au (50/150/200)	E-beam evaporation	n-epi/n^+-bulk (HVPE for epi)	-	1.02	Patterned by lift-off	4×10^{16}	[61]
Ni/Au (20/80)	Ti/Au (20/80)	E-beam evaporation	n-epi/n^+-bulk (HVPE/EFG)	-	-	Patterned by lift-off	$\sim3\times10^{16}$	[62]
Ni/Au	Ti/Au (30/150)	-	n-epi/n^+-bulk (HVPE for epi)	1.2 (*I–V*)	1.08	Diluted HF, wet etching	$\sim1.5\times10^{16}$	[63]
ITO (100)	Ti/Au (20/80)	DC sputtering	n-epi/n^+-bulk (HVPE for epi)	1.15 (*I–V*) 1.24 (*C–V*)	~ 1.1	HCl, ozone	$\sim3\times10^{16}$	[64]
Ni/Au (30/250)	Ti/Au (20/80)	E-beam evaporation	n-epi/n^+-bulk (HVPE/EFG)	1.02 (*I–V*) 1.26 (*C–V*)	1.17	Patterned by lift-off	6.9×10^{15}	[65]
W/Au (20/80)	Ti/Au (20/80)	DC sputtering/ E-beam evaporation	n-epi/n^+-bulk (HVPE/EFG)	0.71 (*I–V*)	1.30	HCl, ozone	3.5×10^{16}	[66]
Ni/Au (200)	Ti/Au	E-beam evaporation	n-epi/n^+-bulk (HVPE for epi)	1.23 (*I–V*)	1.05	BOE	1.6×10^{16}	[67]
Ni/Au (20/80)	Ti/Au (20/80)	E-beam evaporation	n-epi/n^+-bulk (HVPE/EFG)	1.1 (*I–V*)	1.08	Patterned by lift-off	$\sim2\times10^{16}$	[68]
Pt/Ti/Au (15/5/500)	Ti/Au (20/230)	Evaporation	n-epi/n^+-bulk (HVPE/EFG)	1.46 (*I–V–T*)	-	Solvent, acid cleaning	1×10^{16}	[69]
Ni/Au (80/420)	Ti/Au	E-beam evaporation	n-epi/n^+-bulk (HVPE/EFG)	1.05 (*I–V*)	1.03	BOE	2.01×10^{15}	[70]
Ni/Au	Ti/Al/Ni/Au	E-beam evaporation	n-epi/n^+-bulk (HVPE/EFG)	0.98 (*I–V*)	1.13	BOE	$\sim1.5\times10^{16}$	[71]
Pt/Ti/Au (15/5/250)	Ti/Au (20/230)	Evaporation	n-epi/n^+-bulk, (HVPE/EFG)	1.09 ~ 1.15 (*I–V*)	~ 1.0	Acid cleaning	1.4×10^{16}	[72]
Ni/Au	Ti/Au	-	n-epi/n^+-bulk, (HVPE for epi)	1.09 (*I–V*)	1.06	-	$2–3\times10^{16}$	[73]
Ni/Au (20/60)	Ti/Au (20/80)	Thermal evaporation	n-epi/n^+-bulk, (HVPE/EFG)	1.27 (*I–V*) 1.38 (*C–V*)	1.14	Solvent, sulfuric-peroxide mixture (SPM)	1×10^{16}	[74]
Ni/Au (80/300)	Ti/Au (20/80)	E-beam evaporation	n-epi/n^+-bulk (HVPE/EFG)	1.14 (*I–V*)	1.02	UV ozone/HCl: DI (1:10)	2.8×10^{16}	[75]
Cr (20)	Ti/Au (50/250)	E-beam evaporation	n-epi/n^+-bulk, (HVPE/EFG)	~ 1.3 (*C–V*)	-	HF, piranha/ solvent	$2.5–3.2\times10^{16}$	[76]
Ni/Au (20/230)	Ti/Au (50/230)	E-beam evaporation	n-epi/n^+-bulk, (HVPE/EFG)	1.15 (*I–V*)	1.09	Patterned by lift-off	$2.4–3.5\times10^{16}$	[77]

[a]Carrier concentration for the layer on which the Schottky contacts are formed, [b]Growth method: Hydride vapor phase epitaxy (HVPE), Edge-defined film-fed growth (EFG), HVPE/EFG: HVPE-grown epilayer on EFG-grown substrate

alternative for transparent electrodes. Graphene/β-Ga_2O_3 contacts has been studied for the applications of photosensors [9, 98–102]. Graphene/β-Ga_2O_3 Schottky contacts have also been applied for other devices. The graphene/β-Ga_2O_3 contact in the double graphene-gate β-Ga_2O_3 metal – semiconductor FET (MESFET) operated in the enhancement-mode were found to have a barrier height of ~ 0.62 eV and an ideality factor of 1.5 [100]. Yan et al. reported the high critical breakdown field of 5.2 MV/cm in β-Ga_2O_3 perpendicular to the (100) crystal plane using a vertical graphene/β-Ga_2O_3 heterostructure [101]. Kim et al. examined high-performance solar-blind photodetectors based on mechanically exfoliated β-Ga_2O_3 flakes and found that their photoresponsivity was enhanced significantly with UV-transparent graphene electrodes [102]. They also suggested that the high optical transparency

Table 4 Summary of Schottky contacts to (100) β-Ga_2O_3 reported in the literature

Schottky contact (thickness: nm)	Ohmic contact (thickness: nm)	Schottky contact deposition	Device structure (Growth method)	$q\phi_B$ (eV)	Ideality factor	Cleaning method	Carrier concentration (cm^{-3})	Refs
Co (30)	Ti/Au (20/100)	E-beam evaporation	n-bulk (CZ)	1.06 (*I–V*) 1.35 (*I–V–T*)	1.06	10% HCl, H_2O_2 boiling	5×10^{17}-	[78]
Pd (20)	Ti/Au (20/100)	E-beam evaporation	n-bulk (CZ)	~ 1.34 (*I–V*) ~ 1.81 (*I–V*)	~ 1.31	10% HCl, H_2O_2 boiling	4.99×10^{17}	[79]
Ni/Au (40/100)	Ti/Au (20/100)	E-beam evaporation	flakes	~ 1.14 (*I–V*)	~ 1.32	Patterned by lift-off	7×10^{16}	[80]
Pt/Ti/Au (20/10/50)	Ti/Au (10/230)	Sputtering	n-bulk (EFG)	1.38 (*I–V–T*)	1.1	Patterned by lift-off ICP etching for ohmic contact	2.3×10^{14}	[81]
Pt/Au (50/150)	Ti/Au (50/250)	E-beam evaporation	n-bulk (EFG)	-	1.09	Patterned by lift-off Solvent	-	[82]
Au (50)	Ga-In	E-beam evaporation	n-bulk (CZ)	1.07 (*I–V*)	1.02	-	$0.6–8\times10^{17}$	[83]
Ni/Au (20/150)	Ti/Au (50/300)	E-beam evaporation	n-epi/n-bulk (CZ)	1.25 (*C–V*)	-	Solvent, ICP etching for ohmic contact	1.76×10^{17}	[84]
Ni/Au (30/200)	Ti/Au (20/100)	E-beam evaporation	n-bulk (EFG)	1.22 (*I–V*) 1.32 (*C–V*)	1.06	Patterned by lift-off	1.3×10^{17}	[85]
Ni/Au (30/100)	Ti/Au (30/100)	E-beam evaporation	n-bulk (EFG)	0.93 (*I–V*)	1.34	Patterned by lift-off	4.36×10^{17}	[86]

[a]Carrier concentration for the layer on which the Schottky contacts are formed), [b]Growth method: Czochralski (CZ), Edge-defined film-fed growth (EFG)

of graphene gate prevents the shadowing effect under UV–C illumination, enabling carriers to be generated at the graphene/β-Ga_2O_3 junction. Using the first-principles calculations, Yuan et al. suggested the following points in graphene/β-Ga_2O_3 contacts [103]: (1) the small n-type Schottky barrier of ~ 0.07 eV is irrespective of the interface stacking arrangement and the intrinsic electronic property of Ga_2O_3 hardly alters in the interface, (2) the n-type Schottky barrier to ohmic contact transition can be obtained by shorting the interlayer distance, or increasing the graphene layers or applying a negative external electric field, and (3) applying a large positive external electric field can realize the p-type Schottky barrier to ohmic contact transition. These results will expand the application of graphene/β-Ga_2O_3 based devices further.

4.2 Ohmic contacts to β-Ga_2O_3

In order to realize high performance devices, it is essential to obtain good ohmic contact with low resistance and high thermal stability/reliability. High quality ohmic contact to β-Ga_2O_3 can be formed when the Schottky barrier is low and/or the β-Ga_2O_3 layer is heavily doped for the carriers to tunnel through the barrier. In general, the specific contact resistivity (ρ_C), typically expressed in $\Omega\cdot cm^2$, is used as a parameter to assess the quality of ohmic contacts [104, 105]. The most common ohmic contacts to β-Ga_2O_3 are composed of Ti/Au metallization with post deposition annealing. Table 6 shows the research results on ohmic contacts to β-Ga_2O_3 in the literature.

As a way of improving ohmic contact properties, Si-ion implantation was employed to create a heavy doped n^+-region that facilitates electron tunneling across the junction [106–108, 110, 111]. However, this process requires high temperature annealing (> 900 °C) to electrically activate Si donors. Ozone molecular beam epitaxy (MBE) was also used to grow highly doped epitaxial layer [112]. Meanwhile, Yao et al. reported that the contact resistance of Ti/Au metallization is associated with the limited interfacial reactions between the metal and β-Ga_2O_3 [113]. They observed that Ti began to react with the Ga_2O_3 at annealing temperatures above 400 °C and formed an insulating oxide layer, increasing the contact resistance. In addition, they investigated the ohmic properties of nine metals (Ti, In, Ag, Sn, W, Mo, Sc, Zn and Zr) with an Au capping layer and concluded that metal work function is not

Table 5 Summary of Schottky contacts to (010) β-Ga_2O_3 reported in the literature

Schottky contact (thickness: nm)	Ohmic contact (thickness: nm)	Schottky contact deposition	Device structure (Growth method)	$q\phi_B$ (eV)	Ideality factor	Cleaning method	Carrier concentration (cm^{-3})	Refs
Pt/Au	Ti/Al/Ti/Au	E-beam evaporation	n-bulk (EFG)	1.20 (*I–V*) 1.30 (*C–V*)	1.55	ICP etching for ohmic contact	4.3×10^{18}	[21]
Ni/Au (50/150)	Ti/Au (50/50)	E-beam evaporation	n-bulk (VGF)	1.27 (*I–V*) 1.50 (*C–V*)	1.16	Solvent, Piranha	1.1×10^{18}	[22]
Ni/Au (20/100)	Sn	E-beam evaporation	n-epi/n^+-bulk (EFG)	0.95 (*I–V*)	3.38	-	-	[87]
Ni (8)	Ti/Al/Ti/Au (total ~ 430)	E-beam evaporation	n-bulk (EFG)	1.50 (*I–V*) 1.54 (*C–V*)	1.04	RIE etching for ohmic contact	$\sim1.1\times10^{17}$	[88]
Ni/Au (10/30)	Ti/Au (100/100)	Evaporation	n-bulk $(0\bar{1}0)$ (EFG)	1.08 (*I–V*)	1.1	-	$1–2.5\times10^{17}$	[89]
Pt/Ti/Au (20/10/30)	Ti/Au (20/40)	Magnetron sputtering	n-bulk (EFG)	1.10 (*I–V*)	1.16	Oxygen plasma for ohmic contact	$2.29–2.31\times10^{17}$	[90]
Pt/Ti/Au (15/5/250)	Ti/Au (20/230)	Evaporation	n-bulk (FZ)	1.36 (*I–V*) 1.52 (*C–V*)	-	Solvent, 46% HF, $H_2SO_4+H_2O_2$	3×10^{16}	[91]
Pt/Au/Ni	Ti/Au/Ni	E-beam evaporation	n-epi/n^+-bulk (LPCVDfor epi)	1.5 (*C–V*)	1.03	ICP-RIE etching for patterning	2.5×10^{17}	[92]
Pt/Au (40/30)	Ti/Au (30/120)	E-beam evaporation	n-epi/n^+-bulk (MOCVD for epi)	-	1.01	ICP etching for sidewall Schottky	1×10^{15}	[93]

[a] Carrier concentration for the layer on which the Schottky contacts are formed, [b] Growth methods: Czochralski (CZ), Edge-defined film-fed growth (EFG), Vertical gradient freeze (VGF), Floating zone (FZ), Low pressure chemical vapor deposition (LPCVD), Metal organic chemical vapor deposition (MOCVD)

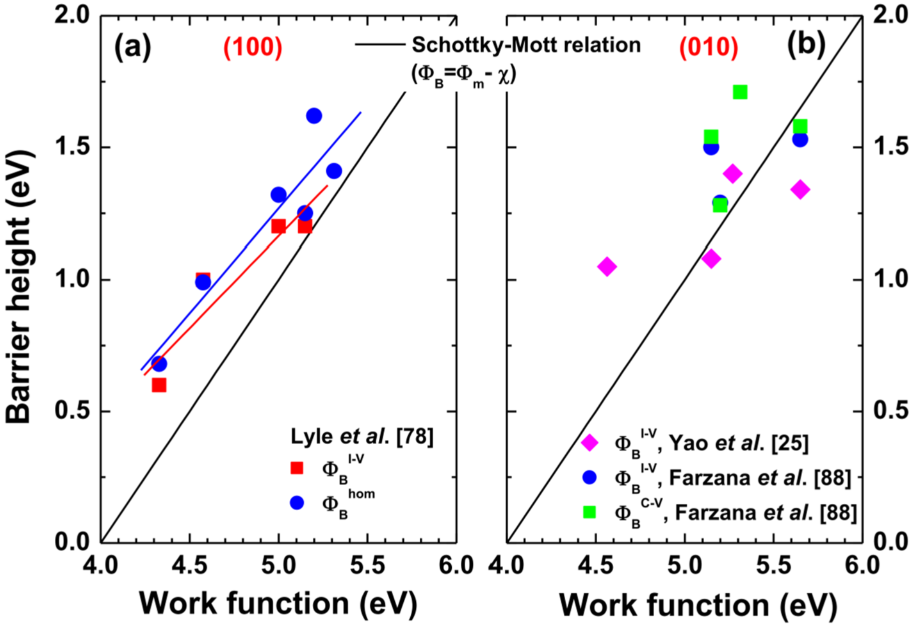

Fig. 4 Plots of barrier height versus metal work function for **a** (100) β-Ga_2O_3 Schottky contacts using the barrier heights taken from Lyle et al. [78] and **b** (010) β-Ga_2O_3 Schottky contacts using the barrier heights taken from Yao et al. [25] and Farzana et al. [88]. The metal work functions were taken from ref. [24]

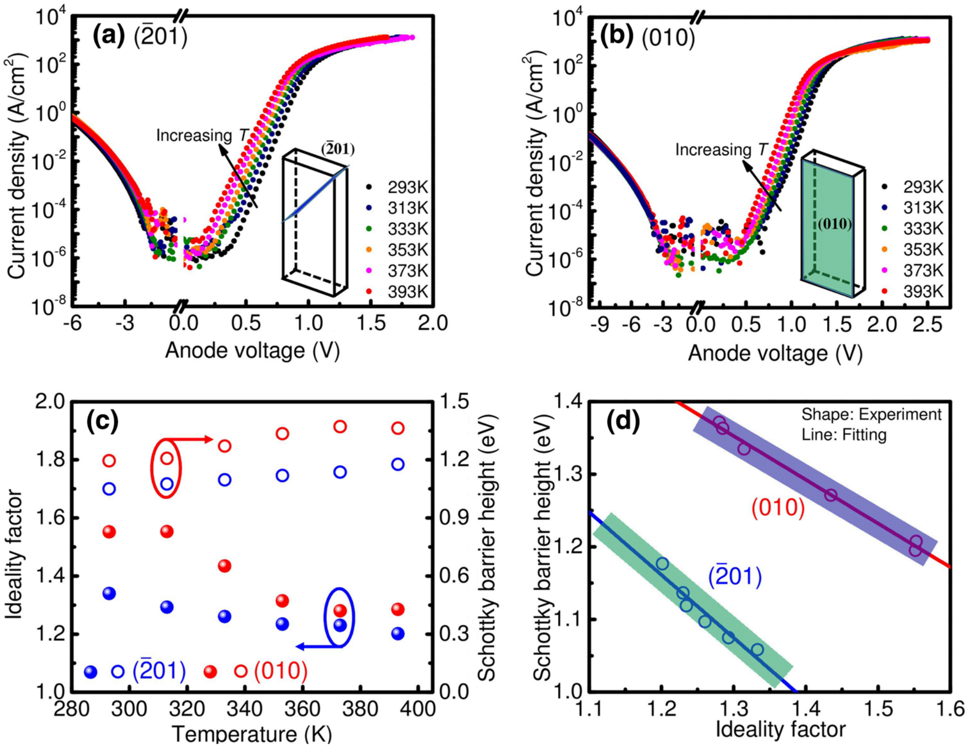

Fig. 5 Temperature-dependent *I*–*V* characteristics for **a** ($\bar{2}$ 01) β-Ga_2O_3 Schottky diode and **b** (010) β-Ga_2O_3 Schottky diode, **c** ideality factor and SBH as a function of temperature, and **d** SBH versus ideality factor [21]

dominant in determining ohmic contact to β-Ga_2O_3 but interfacial reaction gives a significant effect on the morphology and electrical behavior. Li et al. could suppress the contact resistance between Ti and Ga_2O_3 by annealing in Ar ambient [114]. However, they also observed the degraded contact property when annealed above 500 °C. This was associated with the formation of a thicker TiO_x non-/low conductive layer [115]. Therefore, most works utilized the annealing temperature between 400 and 500 °C for the Ti/Au ohmic contact. Lee et al. carried out a study on the interdiffusion and interfacial reactions of the ohmic contact between Ti/Au and β-Ga_2O_3 [116]. As shown in Fig. 7, they could observe a defective β-Ga_2O_3 layer, a Ti–TiO_x layer, and an intermixed Au–Ti layer containing Ti–rich nanocrystalline products after annealing. After insitu annealing with O pressure of 100 Pa at 800 °C for 2 h, Guo et al. observed that the contact exhibited a conversion from ohmic behavior to Schottky behavior, associated with the decrease of concentration of oxygen vacancies [117]. The instability of the Ti/β-Ga_2O_3 interface using Ti/Au metal scheme needs to be improved with enhanced thermal stability. Hence, more comprehensive understanding of interfacial reactions can increase the potential of Ti based ohmic contacts.

Including Si ion implantation, plasma bombardment and reactive ion etching (RIE) has also been studied as other pretreatments prior to the metallization. Higashiwaki et al. showed that the Schottky-like Ti/Au contacts became ohmic-like with the RIE process, which were associated with the generation of oxygen vacancies resulted from the out-diffusion of the oxygen atoms [118]. Zhou et al. also demonstrated that Ar plasma bombardment for 30 s could reduce the contact resistance by enhancing surface n-type doping [119]. Using both RIE and Si ion implantation, the specific contact resistance was reported to be 8.1×10^{-6} Ω·cm^2 [120]. This suggests that the ohmic contact properties can be enhanced by using both RIE and Si ion implantation. Surface defects are introduced at the β-Ga_2O_3 surface during the RIE etching and ion bombardment. Then, these defects can act as carrier recombination centers after metallization, reducing contact resistance. As another method to heavily dope β-Ga_2O_3, Zeng et al. employed spin-on-glass (SOG) method with a high-temperature diffusion drive-in process at 1200 °C for 5 min to obtain heavy Sn-doped β-Ga_2O_3 [121]. The specific contact resistance was found to be ~ 2.1×10^{-5} Ω·cm^2. Xia et al. reported a contact resistance of ~ 1.5 Ω·mm by using a recess and MBE regrown Si delta doping with a carrier concentration of ~ 2×10^{20} cm $^{-3}$ [122]. Based on the reported results, it is speculated that a heavily doped β-Ga_2O_3 layer can be obtained by various doping techniques, resulting in the specific contact resistance of 10^{-5} ~ 10^{-6} Ω·cm^2.

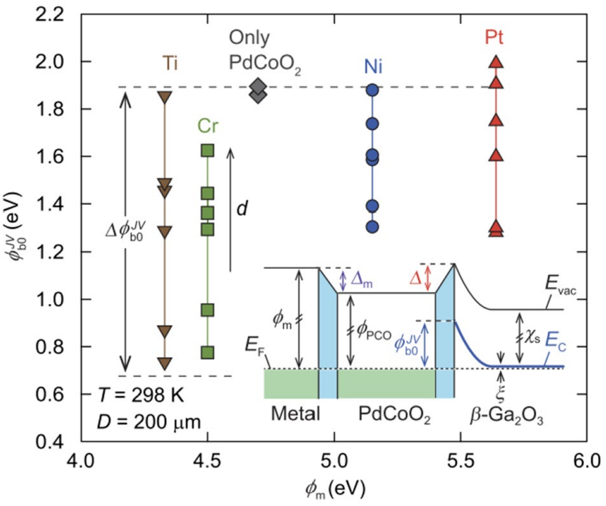

Fig. 6 Plots of barrier height versus metal work function for metal/β-Ga$_2$O$_3$ contacts with an PdCoO$_2$ interlayer (IL). With increasing the thickness d of PdCoO$_2$ IL from 0 to 20 nm, the barrier height was found to increase. The inset shows the possible band diagram with a PdCoO$_2$ (IL). (Reprinted from ref. 97, under the terms of the Creative Commons CC BY 4.0 license)

As shown in Table 6, some works employed indium tin oxide (ITO) and aluminum zinc oxide (AZO) as an IL between ohmic metals and β-Ga$_2$O$_3$ layer [107, 108]. This ohmic contact scheme can be realized with a relatively low doping concentration (~ 10^{17} cm^{-3}) of β-Ga$_2$O$_3$ by post-annealing alone and maintain their ohmic property even after annealing above 1150 °C [108]. These are advantageous compared to Ti-based electrodes, simplifying the device fabrication process and realizing high-temperature operating devices. As shown in Fig. 8, no bubbling was observed on the surface of ITO/Ti/Au contacts while a bubble was observed after annealing at 500 and 600 °C, resulted from the out-diffusion of oxygen atoms into the upper metal layers [110]. Thus, it is required to cap ITO layers with different metal layers to prevent the degradation of surface morphology.

Recently, Lyle et al. fabricated Ti/Au metal contacts on (010) and (001) β-Ga$_2$O$_3$ layers and investigated the interfacial characteristics as a function of annealing temperature [26]. They observed significant differences in the chemical and electrical properties of the Ti/(010) β-Ga$_2$O$_3$ and Ti/(001) β-Ga$_2$O$_3$ interfaces: 1) larger amounts of Ti-oxidation observed on the (001) surface, 2) higher barrier heights on the (010) surface, and 3) changes in the barrier heights for higher temperature annealing and the increase in Ti-oxidation with increasing the temperature. Based on these results, they suggested that the electrical properties of Ti-based contacts depend on the orientation of β-Ga$_2$O$_3$ layer. However, such comparison between different crystal orientations is still lacking and thus more systematic study on the orientation-dependent ohmic contact properties is necessary.

To develop the ohmic contact properties further for n-type β-Ga$_2$O$_3$, the work function of contact metal should be close or smaller than the electron affinity of β-Ga$_2$O$_3$ (4.0 eV [1, 83]). Accordingly, low work function metals such as Hf (work function 3.9 eV), Sc and La (both 3.5 eV) and Gd (2.9 eV) and bilayers of these with Au can be considered as alternatives to Ti/Au [123]. Shi et al. investigated the ohmic contact properties using Mg/Au metallization [124], where the work function of Mg is 3.66 eV [24].

Like Schottky contact, the transport mechanisms for ohmic contact make us to understand the electrical properties of ohmic contacts to β-Ga$_2$O$_3$ thoroughly. According to TE, thermionic field emission (TFE), and field emission (FE) models, the specific contact resistivities are described as [104, 105]

$$\rho_C \propto \frac{1}{T}\exp\left(\frac{q\phi_B}{kT}\right),\ \text{for TE} \tag{6}$$

$$\rho_C \propto \exp\left(\frac{q\phi_B}{E_{00}}\right),\ \text{for TFE \& FE} \tag{7}$$

Here, $E_{00} = q\hbar/2(N_D/m_e\varepsilon_S)^{1/2}$ is the energy parameter, where m_e is the electron effective mass. The current transport mechanism is different according to the E_{00} value, such as TE for $E_{00}/kT < < 1$, TFE for $E_{00}/kT \sim 1$, and FE for $E_{00}/kT > > 1$ [104]. When no significant temperature dependence of the contact resistance is observed, it would imply that the FE model is dominant. In spite of the importance, clarifying the current transport mechanism in β-Ga$_2$O$_3$ ohmic contact has rarely been done. As an example, Shi et al. [125] investigated the carrier transport mechanism of Mg/Au ohmic contact to lightly doped $(\bar{2}\,01)$ β-Ga$_2$O$_3$. They found that the basic mechanism of current transport is dominated by TE model with the effective barrier height of 0.1 eV.

To summarize this section, following points are suggested to be investigated further. Ion implantation requires a high-temperature annealing process to activate the implanted donor, which may cause incomplete activation and surface roughening. Epitaxial growth can produce a high quality of epitaxial layer, but it has some drawbacks such as high expense and low throughput. Hence further studies are necessary to optimize the heavy doping process of β-Ga$_2$O$_3$. Though Ti/Au metallization is widely used for ohmic contacts, other metallization can be investigated. For GaN, Ti/Al/X/Au (X = Ti, Ni, Pt…) multilayers were reported to be good ohmic contacts [126]. Some materials such as TiO$_2$, ITO and AZO reveal the negative conduction band offset (ΔE$_C$) with β-Ga$_2$O$_3$ [127]. When such materials are used as an IL, current can flow through the IL without obstruction under the forward bias while

Table 6 Summary of ohmic contacts to β-Ga_2O_3 reported in the literature

Ohmic contact (thickness: nm)	Thermal annealing	Cleaning method	Ga_2O_3 type (Growth method)	ρ_C ($\Omega \cdot cm^2$)	Carrier concentration (cm^{-3})	Brief description	Refs
Ti/Au (50/300)	450 °C, 1 min (N_2 ambient)	Lift-off	n-epi/n-bulk (010) (MBE/FZ)	4.6×10^{-6}	$1–5 \times 10^{19}$	Si-ion implantation on MBE grown epilayer	[106]
Ti/Au (20/230)	470 °C, 1 min (N_2 ambient)	-	n-epi/bulk (010) (MBE for epi)	7.5×10^{-6}	5×10^{19}	Si-ion implantation on MBE grown epilayer, Characterizing enhanced-mode MOSFET	[107]
AZO/Ti/Au (20/20/80)	400 °C (N_2 ambient)	HCl:DI (1:10)	n-bulk $(\bar{2}01)$ (EFG)	2.82×10^{-5}	$\sim 2.2 \times 10^{17}$	Si-ion implantation on bulk, AZO by RF sputtering	[108]
ITO/Pt (140/100)	800 ~ 1200 °C, 30 s (N_2 ambient)	-	n-bulk (010)	-	2×10^{17}	ITO by RF sputtering, linear *I–V* when annealed at 900 ~ 1150 °C	[109]
ITO/Ti/Au (10/20/80)	500, 600 °C, 30 s (N_2 ambient)	HCl:DI (1:1)	n-bulk $(\bar{2}01)$ (EFG)	6.3×10^{-5}	3×10^{17}	Si-ion implantation on bulk, ITO by RF sputtering	[110]
Ti/Au	470 °C, 1 min (N_2 ambient)	Solvent, RIE etching	n-bulk (010) (MBE/EFG)	3.93×10^{-5}	$\sim 3 \times 10^{19}$	Si-ion implantation on bulk, activated at 950/975 °C	[111]
Ti/Au/Ni	520 °C	-	Not reported	2.7×10^{-4}	1.5×10^{19}	MBE grown epilayer on SI substrate	[112]
Mg/Au (820/600)	500 °C, 2 min	Solvent, Piranha	n-bulk $(\bar{2}01)$	2.1×10^{-5}	4×10^{17}	Annealing at 400 °C showed better stability than 500 °C	[124]

. [a]Carrier concentration for the layer on which ohmic contacts are formed, [b]Growth method: Molecular beam epitaxy (MBE), Edge-defined film-fed growth (EFG), Floating zone (FZ). MBE/FZ (EFG): MBE-grown epilayer on FZ (EFG)-grown substrate

electrons can tunnel through the triangular barrier at the IL/β-Ga_2O_3 interface under the reverse bias, increasing the current values [127]. Therefore, ohmic contact properties with an optimized IL is expected to reduce the ohmic contact resistance further. Like dry plasma etching, wet etching can also affect the ohmic contact properties. Studies on the effect of wet etching on β-Ga_2O_3 ohmic contacts are lacking, requiring further investigations.

5 Reverse leakage current in β-Ga_2O_3

When the defects are present in the semiconductor, they can increase the reverse leakage current and decrease the breakdown voltage. Recently, much research has been done to clarify the relationship between defects and reverse leakage current in β-Ga_2O_3 Schottky diodes. Based on the analysis on the leakage current in Schottky diode array formed on (010) β-Ga_2O_3, Kasu et al. [89] found that the dislocation defects along the [010] direction acted as leakage current sources while Si doping concentration was not associated with the leakage current. In another work, Kasu et al. [128] observed following etch pits on the $(\bar{2}01)$ β-Ga_2O_3 surface: (1) line-shaped etch pattern originated

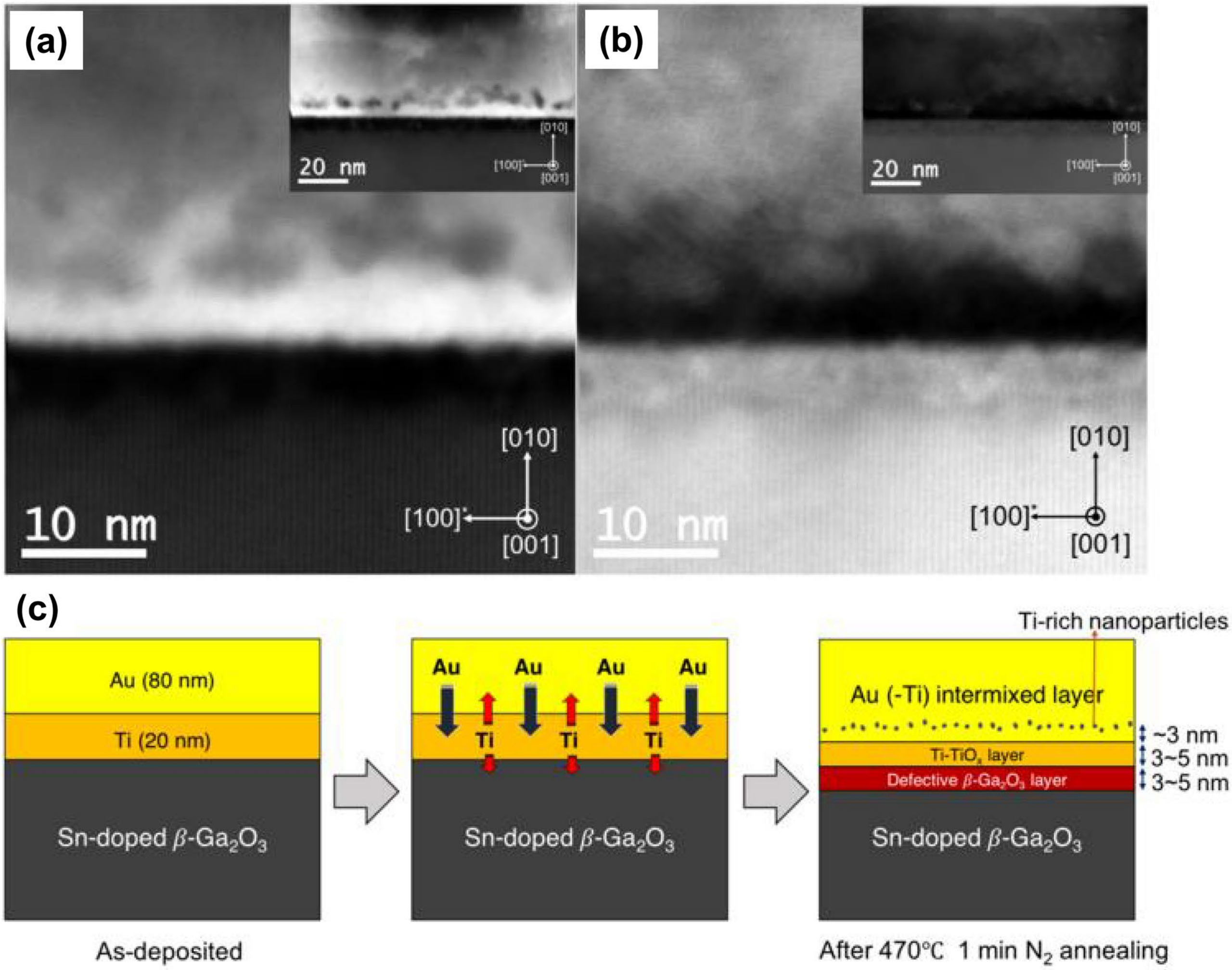

Fig. 7 **a** High-angle annular dark field and **b** bright field scanning transmission electron microscopy (STEM) images of Ti/Au metallization on Sn-doped β-Ga_2O_3 after annealing at 470 °C for 1 min. Insets are the field of view in low magnification. The images show, from the bottom to top, the Ga_2O_3 substrate, a defective Ga_2O_3 region, a Ti-TiO_x region, an Au rich layer, Ti- or TiO_x-rich nanoparticles, and Au-Ti intermixed layer. **c** Schematic illustrations of the evaluation of the Ti/Au metallization layers on Sn-doped β-Ga_2O_3 by thermal annealing. (Reprinted from ref. 116, under the terms of the Creative Commons CC BY 4.0 license)

Fig. 8 Optical micrographs of metal patterns on Au/Ti/ITO/Ga_2O_3 for **a** as-deposited, **b** after 500 °C annealing, and **c** 600 °C annealing [110]

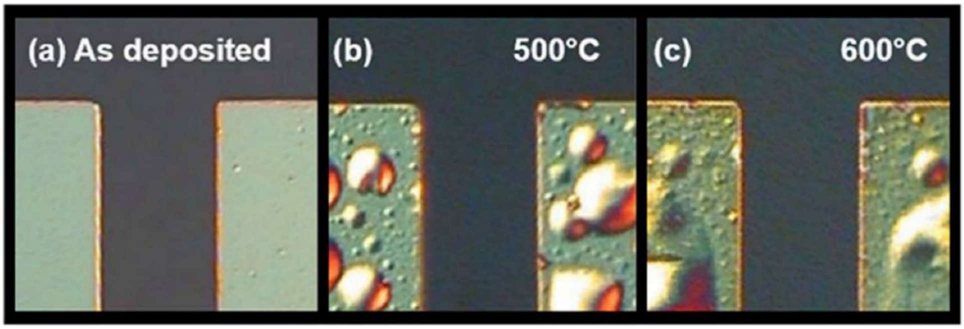

from a void defect and (2) arrow-shaped etch pit and gourd-shaped etch pit originated from a dislocation. Further, they suggested that there is no relationship between the defects and the leakage current in vertical Schottky diodes, unlike the case for the (010) surface. Although the etch pit density on the ($\bar{2}01$) surface was higher than that on the (010) surface, the number of Schottky diodes with a high leakage current was much lower for the $(\bar{2}01)$ surface compared to the (010) surface.

Sdoeung et al. utilized ultra-high sensitive emission microscopy to investigate the origin of reverse leakage current for EFG-grown (001) β-Ga_2O_3 Schottky barrier diodes [129]. They observed that the reverse leakage current is associated with the partially appearing voids on the surface but could not observe clear relationship between the leakage current path and the dislocations by synchrotron X-ray topography. Oshima et al. found in Schottky diodes on (001) β-Ga_2O_3 that the electrical properties such as barrier height, ideality factor and leakage current revealed almost no correlation with the density of the line-shaped voids [130]. Stacking faults, one of the killer defects, were considered to be responsible for the leakage current in Schottky contacts to HVPE-grown (001) β-Ga_2O_3 [131]. These works indicate that the leakage current sources would be different according to the growth methods and crystal orientations.

The transport mechanisms to explain the reverse leakage current include TE, TFE, and FE models. In general, the dominant transport mechanism depends on the doping concentrations: TE for $N_D < 1 \times 10^{17}$ cm^{-3}, TFE for $1 \times 10^{17} < N_D < 1 \times 10^{19}$ cm^{-3}, and FE for $N_D > 1 \times 10^{19}$ cm^{-3}. When the image-force barrier lowering is present, it can also affect the revere leakage current. According to TE and TFE models, following equations can be used to analyze the reverse *I*–*V* characteristics [23, 132, 133]

$$J^{TE} = A^{**}T^2 \exp\left(-\frac{q\phi_B}{kT}\right) \tag{8}$$

$$J^{TFE} = \frac{A^{**}T}{k}\sqrt{\pi E_{00} q \left[V_R + \frac{\phi_B}{\cosh^2(E_{00}/kT)}\right]} \times \exp\left(-\frac{q\phi_B}{E_0}\right) \exp\left(-\frac{qV_R}{\varepsilon'}\right) \tag{9}$$

$$\varepsilon' = \frac{E_{00}}{E_{00}/kT - \tanh(E_{00}/kT)}, E_0 = E_{00}\coth(E_{00}/kT) \tag{10}$$

where $\xi = \sqrt{2qN_D/\varepsilon_S(V_R + V_b - kT/q)}$ is the electric field at the MS interface, and V_R is the reverse bias voltage. The reverse leakage current in Schottky diodes for wide band-gap semiconductors such as GaN, SiC, and diamond is generally explained by TFE rather than TE, in which the relatively large barrier height hinders thermal emission over the Schottky barrier but renders tunneling through the barrier [69]. This explanation can also be considered for β-Ga_2O_3 Schottky diodes.

When the defects are involved with the leakage current, Poole–Frenkel (PF) emission, one-dimensional variable range hopping (1D-VRH), and trap assisted tunneling (TAT) may contribute to the current conduction [134–136]. Fowler–Nordheim (FN) tunneling is another possible transport mechanism, which becomes dominant when the barrier is thin enough (< 10 nm) [135]. The PF emission is associated with the electron emission via a trap state into a continuum of electron states [134, 135]. When the PF emission is the dominant transport mechanism, the reverse current is described by the following equation

$$J \propto \xi \exp\left[-\frac{q\left(\phi_{PF} - \sqrt{q\xi/\pi\varepsilon_0\varepsilon_S^h}\right)}{kT}\right] \tag{11}$$

where ϕ_{PF} is the electron emission energy from the trap and ε_S^h is the relative dielectric permittivity at high frequencies. The 1D-VRH model describes a thermal activation current transport from the metal into the semiconductor occurring along the defect states related with a threading dislocation near or below the Fermi level [47]. The conductivity of the device is given by [136]

$$\sigma = \sigma_0 \exp[-(T_0/T)^{0.5}] \tag{12}$$

where T_0 is the characteristic temperature. When TAT is dominant, the reverse current is expressed as follows [137]

$$J \propto \exp\left(\frac{-8\pi\sqrt{2qm_e}}{3h\xi}\phi_T^{3/2}\right) \tag{13}$$

where ϕ_T is the electron trap energy. The strong electric field within the depletion region reduces the lateral distance between the traps and the available states in the conduction band, substantially increasing the probability of electron tunneling [137]. Figure 9 shows the schematic band diagram of possible reverse leakage current transport mechanisms in β-Ga_2O_3 Schottky diodes.

Zhou et al. demonstrated in Pt/$(\bar{2}01)$ β-Ga_2O_3 Schottky contacts that the reverse leakage current is governed by the PF emission with the trap emission energy of ~ 0.7 eV [134]. Yang et al. showed in lateral Pt/$(\bar{2}01)$ β-Ga_2O_3 Schottky diodes that two models including the TAT and 1D-VRH play important roles in the reverse leakage current [47]. Xu et al. reported in Ni/$(\bar{2}01)$ β-Ga_2O_3 Schottky contacts that the TFE and TAT models are dominant at low and high reverse biases, respectively, associated with the deep-level traps at the MS interface [138]. According to the comparative analysis on the Pt/β-Ga_2O_3 Schottky contacts on ($\bar{2}$ 01) and (010) substrates, Fu et al. showed that the reverse current for both samples were explained by the TAT and 1D-VRH models [21].

Lingaparthi et al. observed high reverse leakage current in Ni/(001) β-Ga_2O_3 Schottky diodes [77]. Based on the comparison between experimental and simulation data, they concluded that the thin surface barrier formed by high density of oxygen vacancies near the surface caused tunneling to occur easily. Further, they could reduce the leakage current after annealing in an oxidative environment. Xu et al. showed in Au/β-Ga_2O_3 based metal–semiconductor-metal solar blind photodetectors that the dark reverse leakage current is dominated by the TFE at low electric field and the PF emission from a deep trap level of 0.42 eV at high field, respectively [139]. Xia et al. found in Ni/(001) β-Ga_2O_3 Schottky diodes that the reverse leakage current showed a good fit to the TFE model when the reverse voltage was less than 80 V, and it was dominated by the tunneling effect at higher voltage [67]. They also observed that at high reverse voltage, a large number of electrons are injected into the drift region, and the current follows a trap-assisted space-charge-limited conduction (SCLC) mechanism. Li et al. analyzed the reverse leakage current of Ni/($\bar{2}$ 01) β-Ga_2O_3 Schottky diodes using the numerical reverse leakage model [45]. As shown in Fig. 10(a), they could explain the reverse leakage current, with including both the image-force lowering (IFL) and doping effects. They also observed that the linearity in the FN plot shown in Fig. 10(b) deviated with the temperature, indicating that not FE but TFE is strongly involved. Furthermore, they observed that the barrier height from the reverse leakage model is consistent with those from the forward *I*–*V* and *C*–*V* methods. Based on the analysis, they suggested the possibility of achieving the intrinsic breakdown electric field in β-Ga_2O_3 Schottky diodes with a high barrier height of 2.2 ~ 3 eV, without developing p-n homojunction in Ga_2O_3 [45]. To data, however, the analysis on the reverse leakage current in β-Ga_2O_3 Schottky diodes is limited in the literature. Therefore, the development of various β-Ga_2O_3 based devices requires to clarify the exact transport mechanisms in metal/β-Ga_2O_3 contacts.

Using CF_4 plasma treatment, Luo et al. reported the suppression of reverse leakage current by four orders of magnitude in Ni/ β-Ga_2O_3 Schottky diodes [140]. Okumura and Tanaka performed wet and dry etchings for β-Ga_2O_3 and investigated various acid and alkali solutions to remove the plasma-induced damage [141]. By immersing the plasma etched samples in hot phosphoric acid solution, they could find the differential on resistance and the ideality factor of (001) β-Ga_2O_3 Schottky diodes with mesa termination to be 0.91 mΩcm^{-2} and 1.03, respectively, and could explain the reverse current by TFE model. Xia et al. comparatively investigated the effects of downstream plasma exposure with O_2, N_2 and CF_4 on (001) β-Ga_2O_3 substrate and observed that the changes are much less than caused by exposure to hydrogen-containing plasmas [142]. While fabricating Ga_2O_3 based devices, plasma treatments are used in deep etching for patterning, surface cleaning, resist/dielectric layer removing. In those cases, the plasma-induced damage is unavoidable, which degrades the device performance [48, 58, 143, 144]. Thus, an additional process for minimizing the plasma-induced surface damage is crucial to realize suitable device performance. Yang et al. employed thermal annealing at 450 °C to remove the near-surface damage caused by inductively coupled plasma (ICP) discharges of BCl_3/Ar [145]. To reduce the surface damage of dry etched β-Ga_2O_3, Lee et al. performed the wet etching processes using tetramethyl ammonium hydroxide (TMAH) solution and sulfuric peroxide mixture (SPM) solution [146]. Tang et al. reported high performance β-Ga_2O_3 trench Schottky diodes with the employment of a novel etching technique called self-reactive etching (SRE) [147]. These works suggest that the development of etching and the post etching methods is another important issue in fabricating β-Ga_2O_3 based devices.

Because the thermal stability is critical in the performance of β-Ga_2O_3 based devices, the temperature-dependent *I* – *V* measurements were mainly performed at elevated temperatures [42, 50, 72, 78, 79, 87]. But this does not provide full information about the conduction mechanism and the properties of the barrier formation. The low-temperature dependent *I* – *V* characteristics enable us to understand the different aspects of the transport mechanisms. For instances, Reddy et al. investigated the current characteristics of Au/Ni/β-Ga_2O_3 Schottky diodes in the temperature range of 100 ~ 400 K [65]. Sheoran et al. also characterized the *I* – *V* properties of Au/Ni/β-Ga_2O_3 Schottky diodes in the temperature range of 78 ~ 350 K [74]. For both works, higher ideality factor than unity at low temperatures was explained by the inhomogeneous Schottky barrier. Meanwhile, Labed et al. examined the *I* – *V* characteristics of Ni/β-Ga_2O_3 Schottky contacts in the temperature range of 100 ~ 300 K and concluded that tunneling is reduced while TE is increased with increasing temperature [148]. At low temperatures, tunneling effect becomes more significant in the current conduction [23]. However, there is little research on the low temperature electrical characterization [57, 149], which needs to be considered for future works.

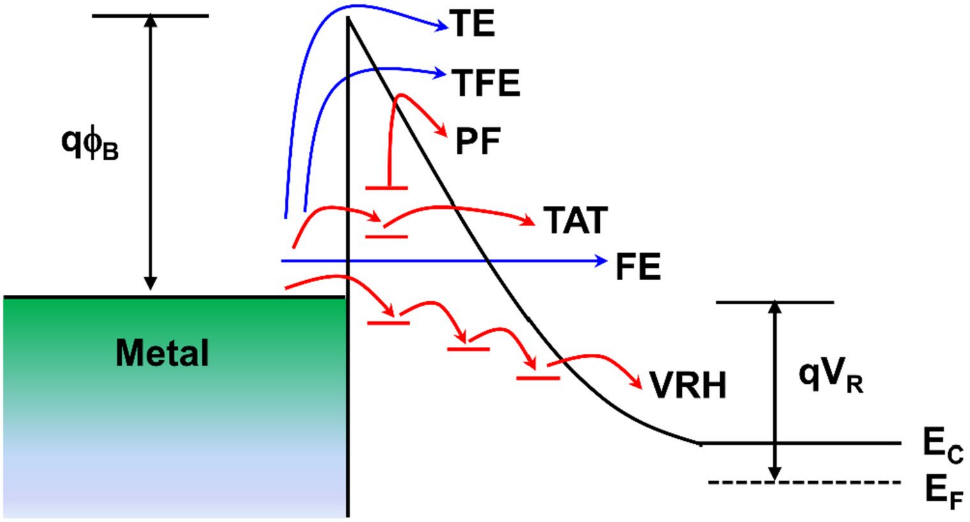

Fig. 9 Schematic band diagram of possible reverse leakage current transport mechanisms in β-Ga_2O_3 Schottky diodes

6 Surface and deep-level defects in β-Ga_2O_3

Because the density of surface/interface states plays an important role in determining the effective SBH, passivating these states is essential to improve the diode performance. Therefore, the nature of surface electronic behavior is also an important factor for metal contacts and gas sensing devices. In n-type semiconductors, the FL is pinned at the charge neutrality level (CNL) at the surface due to surface states, in which the surface barrier height is given by [150]

$$q\phi_B = E_g - E_V \tag{14}$$

where E_V is the valence band maximum (VBM) measured with respect to the FL. Using X-ray photoemission spectroscopy (XPS) measurements, Fu et al. obtained the surface barrier heights of 1.14 and 1.63 eV for the ($\bar{2}$ 01) and (010) β-Ga_2O_3 surfaces, respectively. The conduction bands were bent upward, implying the presence of negatively charged surface states and defects near the surfaces [21]. CNL is located near the middle of the band gap in conventional semiconductors such as Si and GaAs, where the metal induced gap states (MIGS) change from a donor-like to an acceptor-like nature [151, 152]. As shown in Fig. 11, the CNLs for ZnO, CdO, In_2O_3, and SnO_2 are located at 0.5, 0.4, 0.7, and 0.6 eV above the conduction band minimum (CBM), respectively, which can be understood by the relatively low energy of CBM formed by the low-lying metal *s* orbitals [153]. Therefore, the surface states tend to be positively charged donor-like, causing electrons to be accumulated near the surface and a downward band bending is observed. The CNL for Ga_2O_3 is located at 0.6 eV below the CBM, causing both surface electron depletion and upward band bending [154].

Hong et al. performed post deposition annealing at 200 °C for Ni/Au Schottky contacts to (001) β-Ga_2O_3 substrate and found the lower interface trap density and higher reverse breakdown voltage compared to the as-grown sample, which was explained by the NiO formation due to the Ni diffusion into Ga_2O_3 [155]. Hu et al. employed a floating metal ring (FMR) edge termination structure in Ni/Au contacts to β-Ga_2O_3 and found that the interface trap density was in the range of 1.24×10^{12} cm^{-2} eV^{-1} to 1.71×10^{13} cm^{-2} eV^{-1} [80]. Yatskiv et al. investigated the electrical properties of graphite/β-Ga_2O_3 Schottky junctions formed on two different ($\bar{2}$ 01) and (010) β-Ga_2O_3 orientations and found better diode performance for ($\bar{2}$ 01) orientation, associated with a lower density of interface states and their shorter trapping/detrapping time constants [156]. Ingebrigtsen et al. observed the lower reverse leakage current and the lower ideality factor in the (010) samples compared to the ($\bar{2}$ 01) ones. Using deep level transient spectroscopy (DLTS), they found that the E2 concentration (E_C–0.82 eV) in the ($\bar{2}$ 01) samples is higher compared to that in the (010) samples, associated with the different band bending at the two β-Ga_2O_3 surfaces [157]. The barrier heights of the oxidized Schottky contacts were 0.5 ~ 0.8 eV higher than their plain metal counterparts, associated with the passivation of interfacial oxygen vacancies and an increase in the work function of the oxidized metals [56]. With the oxygen annealing, Lingaparthi et al. observed the passivation of surface states and the reduction of the net carrier concentration, lowering the reverse leakage of β-Ga_2O_3 Schottky diodes [158]. These results indicate that the surface/interface states affect the electrical properties of metal/ β-Ga_2O_3 contacts and the passivation effect of these states would be investigated further.

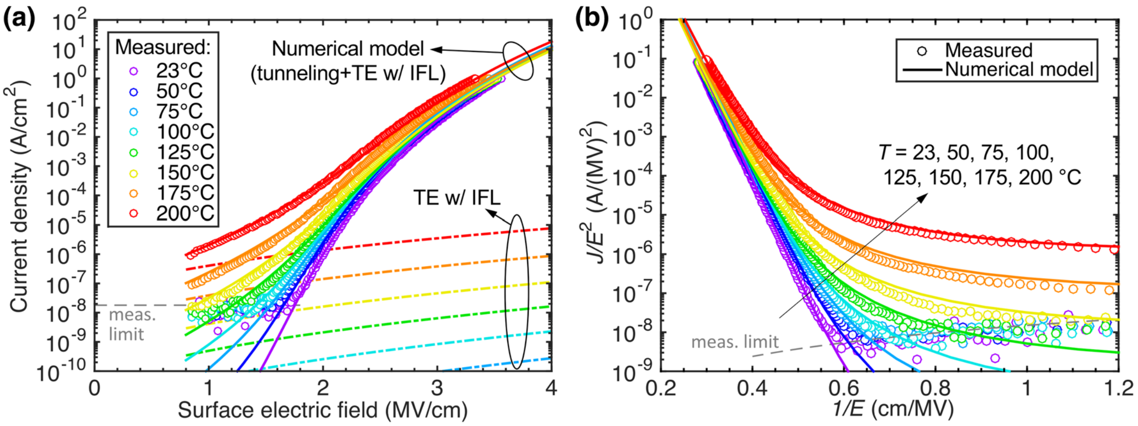

Fig. 10 **a** Temperature-dependent reverse leakage current density, with the numerical reverse leakage model. The contribution from thermionic emission (TE) with image force lowering (IFL) is also shown. **b** Fowler–Nordheim (FN) plot with the fitting results using the numerical reverse leakage model [45]

Using DLTS and deep-level optical spectroscopy (DLOS) measurements, Zhang et al. investigated the deep-level defects in EFG-grown (010) β-Ga_2O_3 [159]. They reported that the three traps at E_C–0.62, 0.82, and 1.00 eV are similar to traps in CZ-grown β-Ga_2O_3 observed by Irmscher et al. [160]. It was predicted that Sn on Ga sites (Sn_{Ga}) or oxygen vacancy may be related with the defects at E_C–0.82 eV [159, 161]. According to the temperature-dependent van der Pauw and Hall-effect measurements for the samples grown by various methods, including EFG, CZ, MBE, and low-pressure chemical vapor deposition (LPCVD), Neal et al. reported that the donor energy of Si and Ge is 30 meV, while the acceptor energies for Fe and Mg are 860 meV and 1.1 eV, respectively [162]. Farzana et al. reported in Ge-doped (010) β-Ga_2O_3 grown by plasma assisted MBE that the dominant deep-level states are in the middle and lower half parts the bandgap, with the highest concentration for energy levels at E_C –2.00 eV, E_C–3.25 eV, and E_C–4.37 eV [163]. This is contrary to the results reporting much higher concentrations of defects within the upper bandgap region [159, 160]. Figures 12(a) and (b) show the summary of the energy distribution of deep level defects for EFG-grown β-Ga_2O_3 (010) substrate and Ge-doped β-Ga_2O_3 (010) MBE epitaxial layers, respectively, by Farzana et al. [163]. Very low concentration of relatively shallow levels in the range of E_C–0.1 eV to E_C–0.2 eV was observed in PAMBE-grown Ge-doped (010) β-Ga_2O_3 epitaxial layers, suggesting high potential for future devices where defect levels in the upper regions are responsible for device degradation mechanisms.

Studies on irradiated samples is also beneficial for identifying and explaining electrically active defects. Ingebrigtsen et al. investigated the impact of proton irradiation on the charge carrier concentration and electrically active defects [164]. Polyakov et al. investigated the effect of hydrogen plasma on deep-level spectra and suggested that hydrogen plasma exposure could produce surface damage in the near-surface region and compensate shallow donors [165]. Ghadi et al. investigated the deep-level defects in metal organic chemical vapor deposition (MOCVD)-grown β-Ga_2O_3 [166]. As a p-type dopant, Mg acceptor levels in MOCVD-grown β-Ga_2O_3 has also been investigated [167]. According to the growth methods, there may exist various deep-level defects in the epitaxial Ga_2O_3 layer. As comprehensively reviewed by Wang et al. [168] and Tadjer et al. [169], the origin of deep-level defects is an important electrical component to be studied. These defects can act as electron traps, affecting the current conduction significantly.

Chen et al. investigated the emission kinetics of a single-trap in ($\bar{2}$ 01) β-Ga_2O_3 Schottky diodes and reported

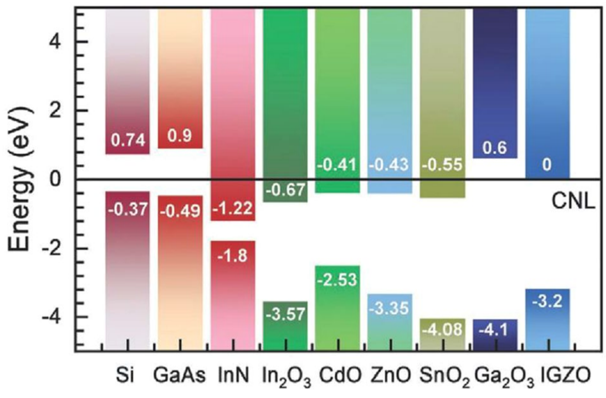

Fig. 11 Band lineups of oxide semiconductors and other conventional semiconductors [153]

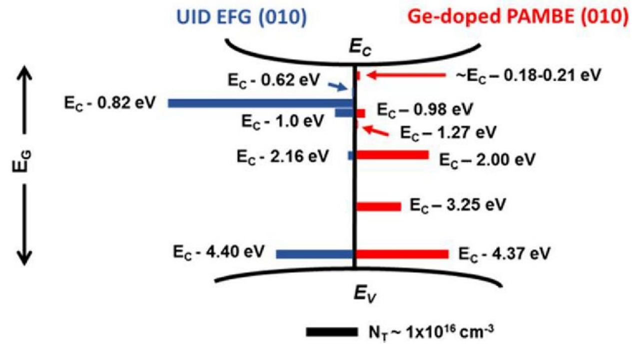

Fig. 12 Summary of the distribution (energy levels and concentrations) of deep-level defects for **a** EFG-grown (010) β-Ga_2O_3 substrate and **b** MBE-grown Ge-doped (010) β-Ga_2O_3 epitaxial layers. The horizontal bars represent the concentration of each trap state, drawn to the scale of 1×10^{16} cm^{-3} as indicated by the black line (N_T) [163]

that the deep level E1 (E_C–0.63 eV) observed by DLTS is related with the PF emission [170]. Based on the temperature-dependent Hall-effect measurements, Oishi et al. found that the dominant scattering mechanisms are ionized impurity and optical phonon scatterings for the low- and high-temperature regions, respectively [171]. Gong et al. fabricated β-Ga_2O_3 Schottky diodes terminated with p-NiO field limiting rings and reported that the reverse leakage mechanism is identified to be PF emission through localized traps with an energy level of E_C–0.72 eV [172], similar to the energy level of gallium vacancies (V_{Ga}) in β-Ga_2O_3 determined by DLTS method [173]. Armstrong et al. observed the strong photoconductive gain in β-Ga_2O_3 Schottky photodiodes and associated it with self-trapped hole formation near the Schottky diode, lowering the effective Schottky barrier in reverse bias and producing photoconductive gain [174]. Qian et al. employed fluorine plasma treatment in Ga_2O_3-based solar-blind photodetectors and found the enhanced device performance due to the passivation of local oxygen vacancies and the suppression of surface chemisorption [175]. However, the detailed mechanism explaining the effect of each defect on the current transport mechanisms is unsatisfactory. Therefore, clarifying the correlation between surface/deep level-defects and current transport mechanisms more thoroughly is suggested for another future work.

7 Summary

Many published review papers regarding β-Ga_2O_3 single crystals in the literature are roughly categorized as follows: 1) growth and material properties of bulk β-Ga_2O_3 [168, 169, 176–181], bulk β-Ga_2O_3-based power/photonic devices [8, 9, 182–185] and their combination [1, 186–190]. Studies on metal contacts are essential to understand the electrical behavior of β-Ga_2O_3-based devices and the material properties of Ga_2O_3. To data, reviews of metal contacts to β-Ga_2O_3 single crystals are still lacking [191, 192]. This review suggests the following further research for metal/ β-Ga_2O_3 contacts: (1) clarifying the correlation between various defects and current transport mechanisms based on the temperature-dependent electrical properties, (2) nanoscale electrical investigation to explain the macroscale electrical properties, (3) controllable n-type heavy doping and thermally stable metallization for ohmic contacts. Resultantly, the importance of studies on the metal contacts to β-Ga_2O_3 (both bulk and epitaxial layers) will increase continuously.

Acknowledgements This study was supported by the Research Program funded by the Seoul National University of Science and Technology (Seoultech).

Declarations

Conflict of interest The author declares that there is no conflict of interest.

References

1. Pearton S, Yang J, Cary P, Ren F, Kim J, Tadjer M, Mastro M (2018) A review of Ga_2O_3 materials, processing, and devices. Appl Phys Rev 5:011301
2. Lin C, Yuda Y, Wong M, Sato M, Takekawa N, Konishi K, Watahiki T, Yamamuka M, Murakami H, Kumagai Y, Higashiwaki M (2019) Vertical Ga_2O_3 Schottky barrier diodes with guard ring formed by nitrogen-ion implantation. IEEE Electron Dev Lett 40:1487–1490
3. Higashiwaki M, Sasaki K, Murakami H, Kumagai Y, Koukitu A, Kuramata A, Masui T, Yamakoshi S (2016) Recent progress in Ga_2O_3 power devices. Semicond Sci Technol 31:034001
4. Xiao M, Wang B, Liu J, Zhang R, Zhang Z, Ding C, Lu S, Sasaki K, Lu G, Buttay C, Zhang Y (2021) Packaged Ga_2O_3 Schottky rectifiers with over 60-A surge current capability. IEEE Trans Power Electron 36:8565

5. Bae J, Kim H, Kang I, Yang G, Kim J (2018) High breakdown voltage quasi-two-dimensional β-Ga$_2$O$_3$ field-effect transistors with a boron nitride field plate. Appl Phys Lett 112:122102
6. Joishi C, Xia Z, McGlone J, Zhang Y, Arehart A, Ringel S, Lodha S, Rajan S (2018) Effect of buffer iron doping on delta-doped β-Ga$_2$O$_3$ metal semiconductor field effect transistors. Appl Phys Lett 113:123501
7. Green A, Chabak K, Heller E, Fitch R Jr, Baldini M, Fiedler A, Irmscher K, Wagner G, Galazka Z, Tetlak S, Crespo A, Leedy K, Jessen G (2016) 3.8-MV/cm breakdown strength of MOVPE-grown Sn-doped β-Ga2O3 MOSFETs. IEEE Electron Dev Lett 37:902
8. Chen X, Ren F, Gu S, Ye J (2019) Review of gallium-oxide-based solar-blind ultraviolet photodetectors. Photonic Res 7:381
9. Guo D, Guo Q, Chen Z, Wu Z, Li P, Tang W (2019) Review of Ga$_2$O$_3$-based optoelectronic devices. Mater Today Phys 11:100157
10. Tomm Y, Ko J, Yoshikawa A, Fukuda T (2001) Floating zone growth of β-Ga$_2$O$_3$: A new window material for optoelectronic device applications. Solar Energy Mater Solar Cells 66:369
11. Suzuki N, Ohira S, Tanaka M, Sugawara T, Nakajima K, Shishido T (2007) Fabrication and characterization of transparent conductive Sn-doped β-Ga$_2$O$_3$ single crystal. Phys Status Solidi C 4:2310
12. Jang S, Jung S, Kim J, Ren F, Pearton S, Baik K (2018) Hydrogen sensing characteristics of Pt Schottky diodes on (2 01) and (010) Ga2O3 single crystals. ECS J Solid State Sci Technol 7:Q3180
13. Guo Z, Verma A, Wu X, Sun F, Hickman A, Masui T, Kuramata A, Higashiwaki M, Jena D, Luo T (2015) Anisotropic thermal conductivity in single crystal β-gallium oxide. Appl Phys Lett 106:111909
14. Cho J, Jung G, Kim K, Kim J, Hong S, Song J, Jang J (2021) Highly asymmetric optical properties of β-Ga$_2$O$_3$ as probed by linear and nonlinear optical excitation spectroscopy. J Phys Chem C 125:1432
15. Chen H, Fu H, Huang X, Montes J, Yang T, Baranowski I, Zhao Y (2018) Characterizations of the nonlinear optical properties for (010) and (2 01) beta-phase gallium oxide. Opt Express 26:3938
16. Liu X, Liu Q, Zhao B, Ren Y, Tao B, Zhang W (2020) Comparison of β-Ga$_2$O$_3$ thin films grown on *r*-plane and *c*-plane sapphire substrates. Vacuum 178:109435
17. Wong M, Sasaki K, Kuramata A, Yamakoshi S, Higashiwaki M (2016) Electron channel mobility in silicon-doped Ga$_2$O$_3$ MOSFETs with a resistive buffer layer. Jpn J Appl Phys 55:1202B9
18. Zhang Y, Mauze A, Speck J (2019) Anisotropic etching of β-Ga$_2$O$_3$ using hot phosphoric acid. Appl Phys Lett 115:013501
19. Jang S, Jung S, Beers K, Yang J, Ren R, Kuramata A, Pearton S, Baik K (2018) A comparative study of wet etching and contacts on (2 01) and (010) oriented β-Ga2O3. J Alloys Compounds 731:118
20. Sasaki K, Kuramata A, Masui T, Víllora E, Shimamura K, Yamakoshi S (2012) Device-quality β-Ga$_2$O$_3$ epitaxial films fabricated by ozone molecular beam epitaxy. Appl Phys Express 5:035502
21. Fu H, Chen H, Huang X, Baranowski I, Montes J, Yang T, Zhao Y (2018) A comparative study on the electrical properties of vertical (-201) and (010) β-Ga$_2$O$_3$ Schottky barrier diodes on EFG single-crystal substrates. IEEE Trans Electron Dev 65:3507
22. Bhattacharyya A, Ranga P, Saleh M, Roy S, Scarpulla M, Llynn K, Krishnamoorthy S (2020) Schottky barrier height engineering in β-Ga$_2$O$_3$ using SiO$_2$ interlayer dielectric. J Electron Dev Soc 8:286
23. Sze S (1981) Physics of semiconductor devices. Wiley, New York
24. Michaelson H (1977) The work function of the elements and its periodicity. J Appl Phys 48:4729
25. Yao Y, Gangireddy R, Kim J, Das K, Davis R, Porter L (2017) Electrical behavior of β-Ga$_2$O$_3$ Schottky diodes with different Schottky metals. J Vac Sci Technol B 35:03D113
26. Lyle L, Back T, Bowers C, Green A, Chabak K, Dorsey D, Heller E, Porter L (2021) Electrical and chemical analysis of Ti/Au contacts to β-Ga$_2$O$_3$. APL Mater 9:061104
27. Kuramata A, Koshi K, Watanabe S, Yamaoka Y, Masui T, Yamakoshi S (2016) High-quality β-Ga$_2$O$_3$ single crystals grown by edge-defined film-fed growth. Jpn J App Phys 55:1202A2
28. Galazka Z, Uecker R, Irmscher K, Albrecht M, Klimm D, Pietsch M, Brützam M, Bertram R, Ganschow S, Fornariet R (2010) Czochralski growth and characterization of β-Ga$_2$O$_3$ single crystals. Cryst Res Technol 45:1229
29. Galazka Z, Uecker R, Klimm D (2017) Scaling-up of bulk β-Ga$_2$O$_3$ single crystals by the Czochralski method. ECS J Solid State Sci Technol 6:Q3007
30. Zhang J, Li B, Xia C, Pei G, Deng Q, Yang Z, Xu W, Shi H, Wu F, Wu Y, Xu J (2006) Growth and spectral characterization of β-Ga$_2$O$_3$ single crystals. J Phys Chem Solids 67:2448
31. Hoshikawa K, Ohba E, Kobayashi T, Yanagisawa J, Miyagawa C, Nakamura Y (2016) Growth of β-Ga$_2$O$_3$ single crystals using vertical Bridgman method in ambient air. J Cryst Growth 447:36
32. Zhou H, Zhang J, Zhang C, Feng Q, Zhao S, Ma P, Hao Y (2019) A review of the most recent progresses of state-of-art gallium oxide power devices. J Semicond 40:011803
33. Mohamed H, Xia C, Sai Q, Cui H, Pan M, Qi H (2019) Growth and fundamentals of bulk β-Ga$_2$O$_3$ single crystals. J Semicond 40:011801
34. Ohira S, Suzuki N, Arai N, Tanaka M, Sugawara T, Nakajima K, Shishido T (2008) Characterization of transparent and conducting Sn-doped β-Ga$_2$O$_3$ single crystal after annealing. Thin Solid Films 516:5763
35. VÍllora E, Shimamura K, Yoshikaw Y, (2008) Electrical conductivity and carrier concentration control in by Si doping. Appl Phys Lett 92:202120
36. Zhou W, Xia C, Sai Q, Zhang H (2017) Controlling n-type conductivity of β-Ga$_2$O$_3$ by Nb doping. Appl Phys Lett 111:242103
37. Onuma T, Fujioka S, Yamaguchi T, Higashiwaki M, Sasaki K, Masui T, Honda T (2013) Correlation between blue luminescence intensity and resistivity in β-Ga$_2$O$_3$ single crystals. Appl Phys Lett 103:2013
38. Dong L, Jia R, Li C, Xin B, Zhang Y (2017) Ab initio study of N-doped β-Ga$_2$O$_3$ with intrinsic defects: the structural, electronic and optical properties. J Alloys Compd 712:379
39. Kumar A, Sharma K, Chand S, Kumar A (2018) Investigation of barrier inhomogeneities in *I-V* and *C–V* characteristics of Ni/n-TiO$_2$/p-Si/Al heterostructure in wide temperature range. Superlattice Microstruct 122:304
40. Wagner L, Young R, Sugerman A (1983) A note on the correlation between the Schottky-diode barrier height and the ideality factor as determined from *I-V* measurements. IEEE Electron Device Lett 4:320
41. Mönch W (1999) Barrier heights of real Schottky contacts explained by metal-induced gap states and lateral inhomogeneities. J Vac Sci Technol B 17:1867
42. Werner J, Guttler H (1991) Barrier inhomogeneities at Schottky contacts. J Appl Phys 69:1522
43. Li A, Feng Q, Zhang J, Hu Z, Feng Z, Zhang K, Zhang C, Zhou H, Hao Y (2018) Investigation of temperature dependent electrical characteristics on Au/Ni/β-Ga$_2$O$_3$ Schottky diodes. Superlattices Microstruct 119:212
44. Yang J, Ahn S, Ren F, Pearton S, Jang S, Kuramata A (2017) High breakdown voltage (−201) β-Ga$_2$O$_3$ Schottky rectifiers. IEEE Electron Dev Lett 38:906
45. Li W, Saraswat D, Long Y, Nomoto K, Jena D, Xing H (2020) Near-ideal reverse leakage current and practical maximum electric field in β-Ga$_2$O$_3$ Schottky barrier diodes. Appl Phys Lett 116:192101

46. Jayawardena A, Ahyi A, Dhar S (2016) Analysis of temperature dependent forward characteristics of Ni/(-201) β-Ga_2O_3 Schottky diodes. Semicond Sci Technol 31:115002
47. Yang T, Fu H, Chen H, Huang X, Montes J, Baranowski I, Fu K, Zhao Y (2019) Temperature-dependent electrical properties of β-Ga_2O_3 Schottky barrier diodes on highly doped single-crystal substrates. J Semicond 40:012801
48. Yang J, Ahn S, Ren F, Khanna R, Bevlin K, Geerpuram D, Pearton S, Kuramata A (2017) Inductively coupled plasma etch damage in (-201) Ga_2O_3 Schottky diodes. Appl Phys Lett 110:142101
49. Heinselman K, Walker P, Norman A, Parilla P, Ginley D, Zakutayev A (2021) Performance and reliability of β-Ga_2O_3 Schottky barrier diodes at high temperature. J Vac Sci Technol A 39:040402
50. Ahn S, Ren F, Yuan L, Pearton S, Kuramata A (2017) Temperature-dependent characteristics of Ni/Au and Pt/Au Schottky diodes on β-Ga_2O_3. ECS J Solid State Sci Technol 6:P68
51. Tadjer M, Wheeler V, Shahin D, Eddy Jr C, Kub F (2017) Thermionic emission analysis of TiN and Pt Schottky Contacts to β-Ga_2O_3. ECS J Solid State Sci and Technol 6:P165
52. Tran H, Le P, Murdoch B, Allen M, McConville C, Partridge J (2020) Temperature-dependent electrical properties of graphitic carbon Schottky contacts to β-Ga_2O_3. IEEE Trans Electron Dev 67:5669
53. Hou C, Gazoni R, Reeves R, Allen M (2021) Dramatic improvement in the rectifying properties of Pd Schottky contacts on β-Ga_2O_3 during their high-temperature operation. IEEE Trans Electron Dev 68:1791
54. Montes J, Kopas C, Chen H, Huang X, Yang T, Fu K, Yang C, Zhou J, Qi X, Fu H, Zhao Y (2020) Deep level transient spectroscopy investigation of ultra-wide bandgap (01) and (001) β-Ga2O3. J Appl Phys 128:205701
55. Fares C, Ren F, Pearton S (2019) Temperature-dependent electrical characteristics of β-Ga_2O_3 diodes with W Schottky contacts up to 500°C. ECS J Solid State Sci Technol 8:Q3007
56. Hou C, Gazoni R, Reeves R, Allen M (2019) Direct comparison of plain and oxidized metal Schottky contacts on β-Ga_2O_3. Appl Phys Lett 114:033502
57. Oishi T, Koga Y, Harada K, Kasu M (2015) High-mobility β-Ga_2O_3 (-201) single crystals grown by edge-defined film-fed growth method and their Schottky barrier diodes with Ni contact. Appl Phys Express 8:031101
58. Yang J, Ahn S, Ren F, Pearton S, Khanna R, Bevlin K, Geerpuram D, Kuramata A (2017) Inductively coupled plasma etching of bulk, single-crystal Ga_2O_3. J Vac Sci Technol B 35:031205
59. Yang J, Ren F, Tadjer M, Pearton S, Kuramata A (2018) 2300V reverse breakdown voltage Ga_2O_3 Schottky rectifiers. ECS J Solid State Sci Technol 7:Q92
60. Yang J, Ren F, Tadjer M, Pearton S, Kuramata A (2018) Ga2O3 Schottky rectifiers with 1 ampere forward current, 650 V reverse breakdown and 26.5 MW.cm–2 figure-of-merit. AIP Adv 8:055026
61. Lu X, Zhang X, Jiang H, Zou X, Lau K, Wang G (2020) Vertical β-Ga_2O_3 Schottky barrier diodes with enhanced breakdown voltage and high switching performance. Phys Status Solidi A 217:1900497
62. Yang J, Chen Z, Ren F, Pearton S, Yang G, Kim J, Lee J, Flitsiyan E, Chernyak L, Kuramata A (2018) 10 MeV proton damage in β-Ga_2O_3 Schottky rectifiers. J Vac Sci Technol B 36:011206
63. Wang B, Xiao M, Yan X, Wong H, Ma J, Sasaki K, Wang H, Zhang Y (2019) High-voltage vertical Ga_2O_3 power rectifiers operational at high temperatures up to 600K. Appl Phys Lett 115:263503
64. Xia X, Xian M, Fares C, Ren F, Tadjer M, Pearton S (2021) Temperature dependent performance of ITO Schottky contacts on β-Ga_2O_3. J Vac Sci Technol A 39:053405
65. Reddy P, Janardhanam V, Shim K, Reddy V, Lee S, Park S, Choi C (2020) Temperature-dependent Schottky barrier parameters of Ni/Au on n-type (001) β-Ga_2O_3 Schottky barrier diode. Vacuum 171:109012
66. Xian M, Fares C, Ren F, Gila B, Chen Y, Liao Y, Tadjer M, Pearton S (2019) Effect of thermal annealing for W/β-Ga_2O_3 Schottky diodes up to 600 °C. J Vac Sci Technol B 37:061201
67. Xia X, Xian M, Carey P, Fares C, Ren F, Tadjer M, Pearton S, Tu T, Goto K, Kuramata A (2021) Vertical β-Ga_2O_3 Schottky rectifiers with 750 V reverse breakdown voltage at 600 K. J Phys D: Appl Phys 54:305103
68. Yang J, Ahn S, Ren F, Pearton S, Jang S, Kim J, Kuramata A (2017) High reverse breakdown voltage Schottky rectifiers without edge termination on Ga_2O_3. Appl Phys Lett 110:192101
69. Konishi K, Goto K, Murakami H, Kumagai Y, Kuramata A, Yamakoshi S, Higashiwaki M (2017) 1-kV vertical Ga_2O_3 field-plated Schottky barrier diodes. Appl Phys Lett 110:103506
70. Chen Y, Yang J, Ren F, Chang C, Lin J, Pearton S, Tadjer M, Kuramata A, Liao Y (2019) Implementation of a 900 V switching circuit for high breakdown voltage β-Ga_2O_3 Schottky diodes. ECS J Solid State Sci Technol 8:Q3229
71. Taylor N, Ji M, Pan L, Kandlakunta P, Kravchenko I, Joshi P, Aytug T, Paranthaman M, Cao L (2021) Large area vertical Ga_2O_3 Schottky diodes for X-ray detection. Nuclear Inst Methods Phys Res A 1013:165664
72. Higashiwaki M, Konishi K, Sasaki K, Goto K, Nomura K, Thieu Q, Togashi R, Murakami H, Kumagai Y, Monemar B, Koukitu A, Kuramata A, Yamakoshi S (2016) Temperature-dependent capacitance–voltage and current–voltage characteristics of Pt/Ga2O3 (001) Schottky barrier diodes fabricated on n–Ga2O3 drift layers grown by halide vapor phase epitaxy. Appl Phys Lett 108:133503
73. Yang J, Koller G, Fares C, Ren F, Pearton S, Bae J, Kim J, Smith D (2019) ^{60}Co gamma ray damage in homoepitaxial β-Ga_2O_3 Schottky rectifiers. ECS J Solid State Sci Technol 8:Q3041
74. Sheoran H, Tak B, Manikanthababu N, Singh R (2020) Temperature-dependent electrical characteristics of Ni/Au vertical Schottky barrier diodes on β-Ga_2O_3 epilayers. ECS J Solid State Sci Technol 9:055004
75. Carey IV P, Yang J, Ren F, Sharma R, Law M, Pearton S (2019) Comparison of dual-stack dielectric field plates on β-Ga_2O_3 Schottky rectifiers. ECS J Solid State Sci Technol 8:Q3221
76. Lingaparthi R, Thieu Q, Koshi K, Wakimoto D, Sasaki K, Kuramata A (2020) Surface states on (001) oriented β-Ga_2O_3 epilayers, their origin, and their effect on the electrical properties of Schottky barrier diodes. Appl Phys Lett 116:092101
77. Lingaparthi R, Sasaki K, Thieu Q, Takatsuka A, Otsuka F, Yamakoshi S, Kuramata A (2019) Surface related tunneling leakage in β-Ga_2O_3 (001) vertical Schottky barrier diodes. Appl Phys Express 12:074008
78. Lyle L, Jiang K, Favela E, Das K, Popp A, Galazka Z, Wagner G, Porter L (2021) Effect of metal contacts on (100) β-Ga_2O_3 Schottky barriers. J Vac Sci Technol A 39:033202
79. Jadhav A, Lyle L, Xu Z, Das K, Porter L, Sarkar B (2021) Temperature dependence of barrier height inhomogeneity in β-Ga_2O_3 Schottky barrier diodes. J Vac Sci Technol B 39:040601
80. Hu Z, Zhao C, Feng Q, Feng Z, Jia Z, Lian X, Lai Z, Zhang C, Zhou H, Zhang J, Hao Y (2020) The investigation of β-Ga_2O_3 Schottky diode with floating field ring termination and the interface states. ECS J Solid State Sci Technol 9:025001
81. He Q, Mu W, Dong H, Long S, Jia Z, Lv H, Liu Q, Tang M, Tao X, Liu M (2017) Schottky barrier diode based on β-Ga_2O_3 (100) single crystal substrate and its temperature-dependent electrical characteristics. Appl Phys Lett 110:093503
82. Lu X, Zhou L, Chen L, Ouyang X, Liu B, Xu J, Tang H (2018) Schottky x-ray detectors based on a bulk β-Ga_2O_3 substrate. Appl Phys Lett 112:103502

83. Mohamed M, Irmscher K, Janowitz C, Galazka Z, Manzke R, Fornari R (2012) Schottky barrier height of Au on the transparent semiconducting oxide β-Ga_2O_3. Appl Phys Lett 101:132106
84. Khan D, Gajula D, Okur S, Tompa G, Koley G (2019) β-Ga_2O_3 thin film based lateral and vertical Schottky barrier diode. ECS J Solid State Sci Technol 8:Q106
85. Gao Y, Li A, Feng Q, Hu Z, Feng Z, Zhang K, Lu X, Zhang C, Zhou H, Mu W, Jia Z, Zhang J, Hao Y (2019) High-voltage β-Ga_2O_3 Schottky diode with argon-implanted edge termination. Nanoscale Res Lett 14:8
86. Zhang S, Liu Z, Liu Y, Zhi Y, Li P, Wu Z, Tang W (2021) Electrical characterizations of planar Ga_2O_3 Schottky barrier diodes. Micromachines 12:259
87. Oh S, Yang G, Kim J (2017) Electrical characteristics of vertical Ni/ β-Ga_2O_3 Schottky barrier diodes at high temperatures. ECS J Solid State Sci Technol 6:Q3022
88. Farzana E, Zhang Z, Paul P, Arehart A, Ringel S (2017) Influence of metal choice on (010) β-Ga_2O_3 Schottky diode properties. Appl Phys Lett 110:202102
89. Kasu M, Hanada K, Moribayashi T, Hashiguchi A, Oshima T, Oishi T, Koshi K, Sasaki K, Kuramata A, Ueda O (2016) Relationship between crystal defects and leakage current in β-Ga_2O_3 Schottky barrier diodes. Jpn J Appl Phys 55:1202BB
90. Jian G, He Q, Mu W, Fu B, Dong H, Qin Y, Zhang Y, Xue H, Long S, Jia Z, Lv H, Liu Q, Tao X, Liu M (2018) Characterization of the inhomogeneous barrier distribution in a Pt/(100) β-Ga_2O_3 Schottky diode via its temperature-dependent electrical properties. AIP Adv 8:015316
91. Sasaki K, Higashiwaki M, Kuramata A, Masui T, Yamakoshi S (2013) Ga_2O_3 Schottky barrier diodes fabricated by using single-crystal β-Ga_2O_3 (010) substrates. IEEE Electron Dev Lett 34:493
92. Joishi C, Rafique S, Xia Z, Han L, Krishnamoorthy S, Zhang Y, Lodha S, Zhao H, Rajan S (2018) Low-pressure CVD-grown β-Ga_2O_3 bevel-field-plated Schottky barrier diodes. Appl Phys Express 11:031101
93. Zhang Y, Mauze A, Alema F, Osinsky A, Speck J (2019) Near unity ideality factor for sidewall Schottky contacts on un-intentionally doped β-Ga_2O_3. Appl Phys Express 12:044005
94. Yang J, Sparks Z, Ren F, Pearton S, Tadher M (2018) Effect of surface treatments on electrical properties of β-Ga_2O_3. J Vac Sci Technol B 36:061201
95. DeLucca J, Mohney S, Auret F, Goodman S (2000) Pt Schottky contacts to n-GaN formed by electrodeposition and physical vapor deposition. J Appl Phys 88:2593
96. He M, Cheng W, Zeng F, Qiao Z, Chien Y, Jiang Y, Li W, Jiang L, Wang Q, Ang K, Yu H (2021) Improvement of β-Ga_2O_3 MIS-SBD interface using Al-reacted interfacial layer. IEEE Trans Electron Dev 68:3314
97. Harada T, Tsukazaki A (2020) Control of Schottky barrier height in metal/β-Ga_2O_3 junctions by insertion of $PdCoO_2$ layers. APL Mater 8:041109
98. Wu C, He C, Guo D, Zhang F, Li P, Wang S, Liu A, Wu F, Tang W (2020) Vertical α/β-Ga_2O_3 phase junction nanorods array with graphene-silver nanowire hybrid conductive electrode for high-performance self-powered solar-blind photodetectors. Mater Today Phys 12:100193
99. Wu C, Qiu L, Li S, Guo D, Li P, Wang S, Du P, Chen Z, Liu A, Wang X, Wu H, Wu F, Tang W (2021) High sensitive and stable self-powered solar-blind photodetector based on solution-processed all inorganic $CuMO_2$/Ga_2O_3 pn heterojunction. Mater Today Phys 17:100335
100. Kim J, Kim J (2020) Monolithically integrated enhancement-mode and depletion-mode β-Ga_2O_3 MESFETs with graphene-gate architectures and their logic applications. ACS Appl Mater Interfaces 12:7310
101. Yan X, Esqueda I, Ma J, Tice J, Wang H (2018) High breakdown electric field in β-Ga_2O_3/graphene vertical barristor heterostructure. Appl Phys Lett 112:032101
102. Kim S, Oh S, Kim J (2019) Ultrahigh deep-UV sensitivity in graphene-gated β-Ga_2O_3 phototransistors. ACS Photonics 6:1026
103. Yuan H, Su J, Guo R, Tian K, Lin Z, Zhang J, Chang J, Hao Y (2020) Contact barriers modulation of graphene/β-Ga_2O_3 interface for high-performance Ga_2O_3 devices. Appl Surf Sci 527:146740
104. Yu A (1970) Electron tunneling and contact resistance of metal–silicon contact barriers. Solid State Electron 13:239
105. Ng K, Liu R (1990) On the calculation of specific contact resistivity on ⟨100⟩ Si. IEEE Trans Electron Dev 37:1535
106. Sasaki K, Higashiwaki M, Kuramata A, Masui T, Yamakoshi S (2013) Si-ion implantation doping in β-Ga_2O_3 and its application to fabrication of low-resistance ohmic contacts. Appl Phys Express 6:086502
107. Wong M, Nakata Y, Kuramata A, Yamakoshi S, Higashiwaki M (2017) Enhancement-mode Ga_2O_3 MOSFETs with Si-ion-implanted source and drain. Appl Phys Express 10:041101
108. Carey IV P, Yang J, Ren F, Hays D, Pearton S, Jang S, Kuramata A, Kravchenko I (2017) Ohmic contacts on n-type β-Ga_2O_3 using AZO/Ti/Au. AIP Adv 7:095313
109. Oshima T, Wakabayashi R, Hattori M, Hashiguchi A, Kawano N, Sasaki K, Masui T, Kuramata A, Yamakoshi S, Yoshimatsu K, Ohtomo A, Oishi T, Kasu M (2016) Formation of indium–tin oxide ohmic contacts for β-Ga_2O_3. Jpn J Appl Phys 55:1202B7
110. Carey IV P, Yang J, Ren F, Hays D, Pearton S, Kuramata A, Kravchenko I (2017) Improvement of ohmic contacts on Ga_2O_3 through use of ITO-interlayers. J Vac Sci Technol B 35:061201
111. Lee M, Peterson R (2020) Accelerated aging stability of β-Ga_2O_3–titanium/gold ohmic interfaces. ACS Appl Mater Interfaces 12:46277
112. Zeng K, Vaidya A, Singisetti U (2019) A field-plated Ga_2O_3 MOSFET with near 2-kV breakdown voltage and 520 m $\Omega\cdot cm^2$ on-resistance. Appl Phys Express 12:081003
113. Yao Y, Davis R, Porter L (2017) Investigation of different metals as ohmic contacts to β-Ga_2O_3: comparison and analysis of electrical behavior, morphology, and other physical properties. J Electron Mater 46:2053
114. Li Z, Liu Y, Zhang A, Liu Q, Shen C, Wu F, Xu C, Chen M, Fu H, Zhou C (2019) Quasi-two-dimensional β-Ga_2O_3 field effect transistors with large drain current density and low contact resistance via controlled formation of interfacial oxygen vacancies. Nano Res 12:143
115. Porter L, Hajzus J (2020) Perspectives from research on metal-semiconductor contacts: Examples from Ga_2O_3, SiC, (nano)diamond, and SnS. J Vac Sci Technol A 38:031005
116. Lee M, Peterson R (2019) Interfacial reactions of titanium/gold ohmic contacts with Sn-doped β-Ga_2O_3. APL Mater 7:022524
117. Guo D, Wu Z, An Y, Guo X, Chu X, Sun C, Li L, Li P, Tang W (2014) Oxygen vacancy tuned ohmic-Schottky conversion for enhanced performance in β-Ga_2O_3 solar-blind ultraviolet photodetectors. Appl Phys Lett 105:023507
118. Higashiwaki M, Sasaki K, Kuramata A, Masui T, Yamakoshi S (2012) Gallium oxide (Ga_2O_3) metal-semiconductor field-effect transistors on single-crystal β-Ga_2O_3 (010) substrates. Appl Phys Lett 100:013504
119. Zhou H, Si M, Alghamdi S, Qiu G, Yang L, Ye P (2017) High-performance depletion/enhancement-mode β-Ga_2O_3 on insulator (GOOI) field-effect transistors with record drain currents of 600/450 mA/mm. IEEE Electron Device Lett 38:103
120. Oshima T, Okuno T, Arai N, Suzuki N, Ohira S, Fujita S (2008) Vertical solar-blind deep-ultraviolet Schottky photodetectors based on β-Ga_2O_3 substrates. Appl Phys Express 1:011202
121. Zeng K, Wallace J, Heimburger C, Sasaki K, Kuramata A, Masui T, Gardella J, Singisettiet U (2017) Ga_2O_3 MOSFETs using

spin-on-glass source/drain doping technology. IEEE Electron Device Lett 38:513
122. Xia Z, Joishi C, Krishnamoorthy S, Bajaj S, Zhang Y, Brenner M, Lodha S, Rajan S (2018) Delta doped β-Ga_2O_3 field effect transistors with regrown ohmic contacts. IEEE Electron Device Lett 39:568
123. Mastro M, Kuramata A, Calkins J, Kim J, Ren F, Pearton S (2017) Opportunities and future directions for Ga_2O_3. ECS J Solid State Sci Technol 6:P356
124. Shi J, Xia X, Liang H, Abbas Q, Liu J, Zhang H, Liu Y (2019) Low resistivity ohmic contacts on lightly doped n-type β-Ga_2O_3 using Mg/Au. J Mater Sci Mater Electron 30:3860
125. Shi J, Xia X, Abbas Q, Liu J, Zhang H, Liu Y, Liang H (2019) Current transport mechanism of Mg/Au ohmic contacts to lightly doped n-type β-Ga_2O_3. J Semicond 40:012805
126. Greco G, Iucolano F, Roccaforte F (2016) Ohmic contacts to gallium nitride materials. Appl Surf Sci 383:324
127. Hu Z, Li J, Zhao C, Feng Z, Tian X, Zhang Y, Zhang Y, Ning J, Zhou H, Zhang C, Lv Y, Kang X, Feng H, Feng Q, Zhang J, Hao Y (2020) Design and fabrication of vertical metal/TiO_2/β-Ga_2O_3 dielectric heterojunction diode with reverse blocking voltage of 1010 V. IEEE Trans Electron Dev 67:5628
128. Kasu M, Oshima T, Hanada K, Moribayashi T, Hashiguchi A, Oishi T, Koshi K, Sasaki K, Kuramata A, Ueda O (2017) Crystal defects observed by the etch-pit method and their effects on Schottky-barrier-diode characteristics on (-201) β-Ga_2O_3. Jpn J Appl Phys 56:091101
129. Sdoeung S, Sasaki K, Kawasaki K, Hirabayashi J, Kuramata A, Oishi T, Kasu M (2020) Origin of reverse leakage current path in edge-defined film-fed growth (001) β-Ga_2O_3 Schottky barrier diodes observed by high-sensitive emission microscopy. Appl Phys Lett 117:022106
130. Oshima T, Hashiguchi A, Moribayashi T, Koshi K, Sasaki K, Kuramata A, Ueda O, Oishi T, Kasu M (2017) Electrical properties of Schottky barrier diodes fabricated on (001) β-Ga_2O_3 substrates with crystal defects. Jpn J Appl Phys 56:086501
131. Sdoeung S, Sasaki K, Masuya S, Kawasaki K, Hirabayashi J, Kuramata A, Kasu M (2021) Stacking faults: Origin of leakage current in halide vapor phase epitaxial (001) β-Ga_2O_3 Schottky barrier diodes. Appl Phys Lett 118:172106
132. Padovani F, Stratton R (1966) Field and thermionic-field emission in Schottky barriers. Solid State Electron 9:695
133. Fu K, Fu H, Huang X, Yang T, Cheng C, Peri P, Chen H, Montes J, Yang C, Zhou J, Deng X, Qi X, Smith D, Goodnick S, Zhao Y (2020) Reverse leakage analysis for as-grown and regrown vertical GaN-on-GaN Schottky barrier diodes. IEEE J Electron Dev Soc 8:74
134. Zhou L, Lu X, Chen L, Ouyang X, Liu B, Xu J, Tang H (2019) Leakage current by Poole-Frenkel emission in Pt Schottky contacts on (-201) β-Ga_2O_3 grown by edge-defined film-fed growth. ECS J Solid State Sci Technol 8:Q3054
135. Chiu E (2014) A review on conduction mechanisms in dielectric films. Adv Mater Sci Eng 2014:578168
136. Miller E, Yu E, Waltereit P, Speck J (2004) Analysis of reverse-bias leakage current mechanisms in GaN grown by molecular-beam epitaxy. Appl Phys Lett 84:535
137. Guo X, Zhong Y, Chen X, Zhou Y, Su S, Yan S, Liu J, Sun X, Sun Q, Yang H (2021) Reverse leakage and breakdown mechanisms of vertical GaN-on-Si Schottky barrier diodes with and without implanted termination. Appl Phys Lett 118:243501
138. Xu Y, Chen X, Cheng L, Ren R, Zhou J, Bai S, Lu H, Gu S, Zhang R, Zheng Y, Ye J (2019) High performance lateral Schottky diodes based on quasi-degenerated Ga_2O_3. Chin Phys B 28:038503
139. Xu Y, Chen X, Zhou D, Ren F, Zhou J, Bai S, Lu H, Gu S, Zhang R, Zheng Y, Ye J (2019) Carrier transport and gain mechanisms in β-Ga_2O_3-based metal–semiconductor–metal solar-blind Schottky photodetectors. IEEE Trans Electron Dev 66:2276
140. Luo H, Jiang H, Chen Z, Pei Y, Feng Q, Zhou H, Lu X, Lau K, Wang G (2020) Leakage current reduction in β-Ga_2O_3 Schottky barrier diodes by CF_4 plasma treatment. IEEE Electron Dev Lett 41:1312
141. Okumura H, Tanaka T (2019) Dry and wet etching for β-Ga_2O_3 Schottky barrier diodes with mesa termination. Jpn J Appl Phys 58:120902
142. Xia X, Xian M, Fares C, Ren F, Kim J, Kim J, Tadjer M, Pearton S (2021) Effects of downstream plasma exposure on β-Ga_2O_3 rectifiers. ECS J Solid State Sci Technol 10:065005
143. Polyakov A, Lee I, Miakonkikh A, Chernykh A, Smirnov N, Shchemerov I, Kochkova A, Vasilev A, Pearton S (2020) Anisotropy of hydrogen plasma effects in bulk n-type β-Ga_2O_3. J Appl Phys 127:175702
144. Alfieri G, Mihaila A, Godignon P, Varley J, Vines L (2021) Deep level study of chlorine-based dry etched β-Ga_2O_3. J Appl Phys 130:025701
145. Yang J, Khanna F, Bevlin K, Tung D, Lin J, Lee H, Flitsiyan E, Kuramata L (2017) Annealing of dry etch damage in metallized and bare (-201) Ga_2O_3. J Vac Sci Technol B 35:051201
146. Lee H, Yun H, Shim K, Park H, Jang T, Lee S, Choi C (2020) Improvement of dry etch-induced surface roughness of single crystalline β-Ga_2O_3 using post-wet chemical treatments. Appl Surf Sci 506:144673
147. Tang W, Zhang X, He T, Ma Y, Feng B, Wei X, He G, Zhang S, Huo X, Cai Y, Ding S, Zhang X, Zhang B (2021) Temperature-dependent electrical characteristics of β-Ga_2O_3 trench Schottky barrier diodes via self-reactive etching. J Phys D: Appl Phys 54:425104
148. Labed M, Park J, Meftah A, Sengouga N, Hong J, Jung Y, Rim Y (2021) Low temperature modeling of Ni/β-Ga_2O_3 Schottky barrier diode interface. ACS Appl Electron Mater 3:3667
149. Kabilova Z, Kurdak C, Peterson R (2019) Observation of impurity band conduction and variable range hopping in heavily doped (010) β-Ga_2O_3. Semicond Sci Technol 34:03LT02
150. Reddy P, Bryan I, Bryan Z, Guo W, Hussey L, Collazo R, Sitar Z (2014) The effect of polarity and surface states on the Fermi level at III-nitride surfaces. J Appl Phys 116:123701
151. Hou C, Gazoni R, Reeves R, Allen M (2019) Oxidized metal Schottky contacts on (010) β-Ga_2O_3. IEEE Electron Dev Lett 40:337
152. Vines L, Bhoodoo C, Wenckstern H, Grundmann M (2018) Electrical conductivity of In_2O_3 and Ga_2O_3 after low temperature ion irradiation; implications for intrinsic defect formation and charge neutrality level. J Phys: Condens Matter 30:025502
153. Shi J, Zhang J, Yang L, Qu M, Qi D, Zhang K (2021) Wide bandgap oxide semiconductors: from materials physics to optoelectronic devices. Adv Mater 6:200
154. Swallow J, Varley J, Jones L, Gibbon J, Piper L, Dhanak V, Veal T (2019) Transition from electron accumulation to depletion at β-Ga_2O_3 surfaces: the role of hydrogen and the charge neutrality level. APL Mater 7:022528
155. Hong Y, Zheng X, He Y, Zhang F, Zhang X, Wang X, Li J, Wang D, Lu X, Han H, Ma X, Hao Y (2021) The optimized interface characteristics of β-Ga_2O_3 Schottky barrier diode with low temperature annealing. Appl Phys Lett 119:132103
156. Yatskiv R, Tiagulskyi S, Grym J (2020) Influence of crystallographic orientation on Schottky barrier formation in gallium oxide. J Electron Mater 49:5133
157. Ingebrigtsen M, Vines L, Alfieri G, Mihaila A, Badstubner U, Svensson B, Kuznetsov A (2017) Bulk β-Ga_2O_3 with (010) and (201) surface orientation: Schottky contacts and point defects. Mater Sci Forum 897:755
158. Lingaparthi R, Thieu Q, Sasaki K, Takatsuka A, Otsuka F, Yamakoshi S, Kuramata A (2020) Effects of oxygen annealing of β-Ga_2O_3

epilayers on the properties of vertical Schottky barrier diodes. ECS J Solid State Sci Technol 9:024004
159. Zhang Z, Farzana E, Arehart A, Ringel S (2016) Deep level defects throughout the bandgap of (010) β-Ga_2O_3 detected by optically and thermally stimulated defect spectroscopy. Appl Phys Lett 108:052105
160. Irmscher K, Galazka Z, Pietsch M, Uecker R, Fornari R (2011) Electrical properties of β-Ga_2O_3 single crystals grown by the Czochralski method. J Appl Phys 110:063720
161. Varley J, Weber J, Janotti A, Van de Walle C (2010) Oxygen vacancies and donor impurities in β-Ga_2O_3. Appl Phys Lett 97:142106
162. Neal A, Mou S, Rafique S, Zhao H, Ahmadi E, Speck J, Stevens K, Blevins J, Thomson D, Moser N, Chabak K, Jessen G (2018) Donors and deep acceptors in β-Ga_2O_3. Appl Phys Lett 113:062101
163. Farzana E, Ahmadi E, Speck J, Arehart A, Ringel S (2018) Deep level defects in Ge-doped (010) β-Ga_2O_3 layers grown by plasma-assisted molecular beam epitaxy. J Appl Phys 123:161410
164. Ingebrigtsen M, Kuznetsov A, Svensson B, Alfieri G, Mihaila A, Badstubner U, Perron A, Vines L, Varley J (2019) Impact of proton irradiation on conductivity and deep level defects in β-Ga_2O_3. APL Mater 7:022510
165. Polyakov A, Lee I, Smirnov N, Yakimov E, Shchemerov I, Chernykh A, Kochkova A, Vasilev A, Ren F, Carey IV P, Pearton S (2019) Hydrogen plasma treatment of β-Ga_2O_3: changes in electrical properties and deep trap spectra. Appl Phys Lett 1115:032101
166. Ghadi H, McGlone J, Feng Z, Anhar A, Bhuiyan U, Zhao H, Arehart A, Ringel S (2020) Influence of growth temperature on defect states throughout the bandgap of MOCVD-grown β-Ga_2O_3. Appl Phys Lett 117:172106
167. Feng Z, Anhar A, Bhuiyan U, Kalarickal N, Rajan S, Zhao H (2020) Mg acceptor doping in MOCVD (010) β-Ga_2O_3. Appl Phys Lett 117:222106
168. Wang Z, Chen X, Ren F, Gu S, Ye J (2021) Deep-level defects in gallium oxide. J Phys D: Appl Phys 54:043002
169. Tadjer M, Lyons J, Nepal N, Freitas Jr J, Koehler A, Foster G (2019) Review-theory and characterization of doping and defects in β-Ga_2O_3. ECS J Solid State Sci Technol 8:Q3187
170. Chen J, Luo H, Qu H, Zhu M, Guo H, Chen B, Lv Y, Lu X, Zou X (2021) Single-trap emission kinetics of vertical β-Ga_2O_3 Schottky diodes by deep-level transient spectroscopy. Semicond Sci Technol 36:055015
171. Oishi T, Koga Y, Harada K, Kasu M (2015) High-mobility β-Ga_2O_3 (01) single crystals grown by edge-defined film-fed growth method and their Schottky barrier diodes with Ni contact. Appl Phys Express 8:031101
172. Gong H, Yu X, Xu Y, Chen X, Kuang Y, Lv Y, Yang Y, Ren F, Feng Z, Gu S, Zheng Y, Zhang R, Ye J (2021) β-Ga_2O_3 vertical heterojunction barrier Schottky diodes terminated with p-NiO field limiting rings. Appl Phys Lett 118:202102
173. De Santi C, Fregolent M, Buffolo M, Wong M, Higashiwaki M, Meneghesso G, Zanoni E, Meneghini M (2020) Carrier capture kinetics, deep levels, and isolation properties of β-Ga_2O_3 Schottky-barrier diodes damaged by nitrogen implantation. Appl Phys Lett 117:262108
174. Armstrong A, Crawford M, Jayawardena A, Ahyi A, Dhar S (2016) Role of self-trapped holes in the photoconductive gain of β-gallium oxide Schottky diodes. J Appl Phys 119:103102
175. Qian L, Gu Z, Huang X, Liu H, Lv Y, Feng Z, Zhang W (2021) Comprehensively improved performance of β-Ga_2O_3 solar-blind photodetector enabled by a homojunction with unique passivation mechanisms. ACS Appl Mater Interfaces 13:40837
176. Rafique S, Han L, Zhao H (2017) Ultrawide bandgap β-Ga_2O_3 thin films: growths, properties and devices. ECS Trans 80:203
177. Baldini M, Galazka Z, Wagner G (2018) Recent progress in the growth of β-Ga_2O_3 for power electronics applications. Mater Sci Semicond Process 78:132
178. Tak B, Kumar S, Kapoor A, Wang D, Li X, Sun H, Singh R (2021) Recent advances in the growth of gallium oxide thin films employing various growth techniques–a review. J Phys D: Appl Phys 54:453002
179. Nikolskaya A, Okulich E, Korolev D, Stepanov A, Nikolichev D, Mikhaylov A, Tetelbaum D, Almaev A, Bolzan C, Buaczik Jr A, Giulian R, Grande P, Kumar A, Kumar M, Gogova D (2021) Ion implantation in β-Ga_2O_3: physics and technology. J Vac Sci Technol A 39:030802
180. Zhang J, Shi J, Qi D, Chen L, Zhang K (2020) Recent progress on the electronic structure, defect, and doping properties of Ga_2O_3. APL Mater 8:020906
181. Hou X, Zou Y, Ding M, Qin Y, Zhang Z, Ma X, Tan P, Yu S, Zhou X, Zhao X, Xu G, Sun H, Long S (2021) Review of polymorphous Ga_2O_3 materials and their solar-blind photodetector applications. J Phys D: Appl Phys 54:043001
182. Higashiwaki M, Murakami H, Kumagai Y, Kuramata A (2016) Current status of Ga_2O_3 power devices. Jpn J Appl Phys 55:1202A1
183. Singh R, Lenka T, Panda D, Velpula R, Jain B, Bui H, Nguyen H (2020) The dawn of Ga_2O_3 HEMTs for high power electronics - a review. Mater Sci Semicond Process 119:105216
184. Wong M, Higashiwaki M (2020) Vertical β-Ga_2O_3power transistors: a review. IEEE Trans Electron Dev 67:3925
185. Liu Z, Li P, Zhi Y, Wang X, Chu X, Tang W (2019) Review of gallium oxide based field-effect transistors and Schottky barrier diodes. Chin Phys B 28:017105
186. Xue H, He Q, Jian G, Long S, Pang T, Liu M (2018) An overview of the ultrawide bandgap Ga_2O_3 semiconductor-based Schottky barrier diode for power electronics application. Nanoscale Res Lett 13:290
187. Wang C, Zhang J, Xu S, Zhang C, Feng Q, Zhang Y, Ning J, Zhao S, Zhou H, Hao Y (2001) Progress in state-of-the-art technologies of Ga_2O_3 devices. J Phys D: Appl Phys 54:243001
188. Galazka Z (2018) β-Ga_2O_3 for wide-bandgap electronics and optoelectronics. Semicond Sci Technol 33:113001
189. Kaur D, Kumar M (2021) A strategic review on gallium oxide based deep-ultraviolet photodetectors: recent progress and future prospects. Adv Opt Mater 9:2002160
190. Ping L, Berhanuddin D, Mondal A, Menon P, Mohamed M (2021) Properties and perspectives of ultrawide bandgap Ga_2O_3 in optoelectronic applications. Chin J Phys 73:195
191. Huan Y, Sun S, Gu C, Liu W, Ding S, Yu H, Xia C, Zhang D (2018) Recent advances in β-Ga_2O_3-metal contacts. Nanoscale Res Lett 13:246
192. Lee M, Peterson R (2021) Process and characterization of ohmic contacts for beta-phase gallium oxide. J Mater Res. https://doi.org/10.1557/s43578-021-00334-y